Cell Reports
Physical Science

Article

Performance and durability trade-offs in low-iridium catalyst layers for PEM water electrolysis

Graphical abstract

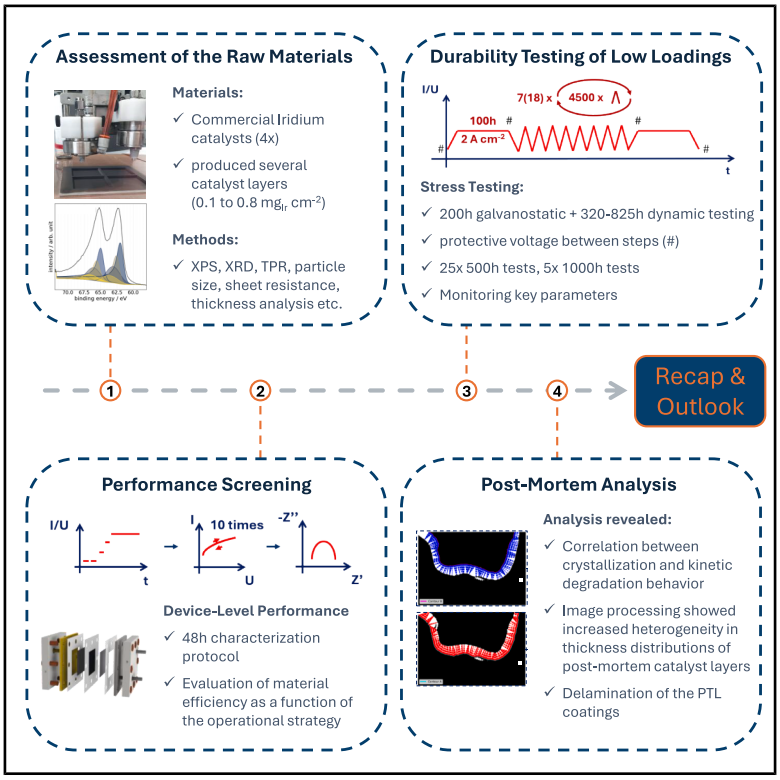

Highlights

- All commercial iridium catalysts meet the 0.1 mg$_{Ir}$ W^{-1} target using N115 membrane
- Cell resistance reduction, not catalyst activity, unlocks 2030 efficiency targets
- Early-stage degradation is most pronounced but decreases with operation time
- Progressive catalyst crystallization explains the kinetic degradation behavior

Authors

Nikolai Utsch, Fabian Scheepers, David Aymé-Perrot, Heinrich Hartmann, Martin Müller, Ralf Peters

Correspondence

n.utsch@fz-juelich.de

In brief

Gigawatt-scale deployment of PEM water electrolyzers demands improved material efficiency, particularly for iridium, a scarce catalyst metal. Utsch et al. show that commercial iridium catalysts already meet power density targets, but 2030 efficiency goals require reducing cell resistance rather than improving catalyst activity, while postmortem analysis reveals progressive crystallization as the key driver of long-term kinetic degradation.

Utsch et al., 2026, Cell Reports Physical Science 7, 103441
August 19, 2026
https://doi.org/10.1016/j.xcrp.2026.103441

CellPress

Cell Reports
Physical Science

CellPress
OPEN ACCESS

Article

Performance and durability trade-offs in low-iridium catalyst layers for PEM water electrolysis

Nikolai Utsch,[1,3,*] Fabian Scheepers,[1] David Aymé-Perrot,[2] Heinrich Hartmann,[1] Martin Müller,[1] and Ralf Peters[1]
[1]Forschungszentrum Juelich GmbH, Institute of Energy Technologies, IET-4, Electrochemical Process Engineering, 52425 Juelich, Germany
[2]TotalEnergies, Tour Coupole - 2 place Jean Millier – La Défense 6, 92078 Paris, France
[3]Lead contact
*Correspondence: n.utsch@fz-juelich.de
https://doi.org/10.1016/j.xcrp.2026.103441

SUMMARY

To deploy proton-exchange membrane (PEM) water electrolyzers at a gigawatt scale, the iridium-specific power density must be reduced to below 0.1 $mg_{Ir}\,W^{-1}$. Significant variability in reported performance and durability benchmarks makes it difficult to define clear pathways for technological improvement. Here, we report a device-level investigation combining multimodal diagnostics with long-term durability testing across four commercial catalysts at loadings from 0.1 to 0.8 $mg_{Ir}\,cm^{-2}$. While all catalysts achieve the 0.1 $mg_{Ir}\,W^{-2}$ target, this cannot be met at lower heating value-based efficiencies above 75% through catalyst design alone. Durability testing over 500 and 1,000 h shows that degradation rates decrease with extended operation and that each catalyst exhibits distinct, loading-dependent behavior. Postmortem characterization confirms progressive catalyst crystallization as a primary contributor to kinetic degradation. These findings demonstrate that future deployment targets depend far more on reducing cell resistance and ensuring long-term durability than on advancing intrinsic catalyst activity.

INTRODUCTION

The increase in demand for metals and minerals is intensifying environmental burdens. Rapidly increasing global metal extraction intensifies greenhouse gas emissions and land-use, water, and biodiversity impacts.[1–4] Clean energy devices are heavily dependent on metals mined, shifting resource dependence from fossil fuels to critical raw materials (CRMs).[5,6] Many decarbonization strategies focus on producing green hydrogen through the use of electrolyzer technologies, either alkaline water electrolysis (AWE) or proton-exchange membrane water electrolysis (PEMWE), combined with renewable energy.

In PEMWE, platinum-group metals (PGMs) are primarily used, which are on a different trajectory in terms of scarcity, costs, and average annual global production (456 t a^{-1}, 2016–2020) than many other metals.[7] According to the Raw Materials Information System (RMIS)[8] of the European Commission (EC), South Africa is, with 60%, the world's main primary producer for PGMs, followed by the Russian Federation (23%). The remaining share is distributed among Zimbabwe (6.5%), Canada (4.5%), the USA (4.1%), China (0.80%), the EU (0.50%, mainly Finland), and a few others. However, in 2021, only 1.7% of global PGM production was attributed to iridium, as it is a sub-product of platinum mining, which is equal to an average global annual production (2016–2020) of 7.54 t a^{-1}.[8] The iridium (or PGM) supply chain is dominated by a few vertically integrated miners and refiners. Global primary PGM supply in 2021 was concentrated, with 89% originating from four South African producers (Anglo American Platinum, Impala Platinum, Sibanye-Stillwater, and Northam Platinum), while additional production came from Zimbabwe (Zimplats) and Russia (MMC Norilsk Nickel PJSC). Iridium-based anode catalysts are hard to replace and are currently not replaceable in PEMWE systems.[9] A small group of global players, including Johnson Matthey (United Kingdom), Heraeus (Germany), BASF (Germany), Umicore (Belgium), and Tanaka (Japan), dominate the market for fabricated products from PGMs with their major refining and catalyst manufacturing capabilities. These companies account for approximately 85% of the market.[7] Some other companies providing iridium electrocatalyst are Ames Goldsmith Corporation (USA), 3M (USA), Dongguan SAT Nano Technology Material (China), Furuya Metal (Japan), Ishifuku Metal Industry (Japan), and CENmat (Germany).

Because there is a wide range of projections for future PEMWE capacity, meaning the future market is uncertain, it is difficult to estimate the demand for iridium for PEMWE systems. The EC anticipates that PEMWE will account for approximately 45% of global electrolyzer deployment by 2030 (compared to 48% for AWE) and decrease to 30% by 2050 (while AWE increases to 44%). Similar proportions are expected in the European market.[10] Clapp et al. modeled capacity requirements based on different International Energy Agency (IEA) scenarios (Announced Pledge Scenario [APS] and Net Zero Emission [NZE] scenario), estimating a need

for 80–220 GW by 2030 and 580–1,130 GW by 2050 by assuming a PEMWE market share of 40%. This large discrepancy clearly propagates into iridium demand projections. For example, the German Mineral Resources Agency (DERA) estimated the global demand for iridium in PEMWE systems to range from 10 to 34 t a^{-1}, depending on the chosen socioeconomic scenario (SSP2 or SSP4). The EC made similar estimates, projecting 9–34 t a^{-1} globally and 2–9 t a^{-1} for the EU.

Clapp et al.[11] considered it both realistic and feasible to allocate around 20% of global primary iridium production (ca. 1.5 t a^{-1}) to the PEMWE sector. An essential step toward meeting the ambitious deployment targets is implementing effective iridium recycling strategies. While the current end-of-life recycling rate (EoL-RR) for iridium is between 20% and 30%.[12] Clapp et al. projected a linear increase in recycling efficiency under industrial application, rising from 70% in 2020 to 100% by 2050.[11] Supporting this outlook, Carmo et al.[13] claimed in 2019 an RR of 97% for iridium recovered from EoL catalyst-coated membranes (CCMs). The noble characteristics of PGMs generally result in high recyclability. For instance, platinum and palladium already achieve recovery rates of over 95%.[7] However, several interrelated uncertainties obscure a robust risk assessment and hinder the formulation of effective mitigation strategies. These include changing ore grades,[14,15] environmental and permitting barriers to new mines,[16–18] shifts in PGM market sectors (e.g., declining use in automobiles counterbalances increased demand from other sectors),[19] and the temporal mismatch between planned hydrogen capacity, demand, and installed production capacity.[20,21] Odenweller et al. found that the absence of a final investment decision (FID) was a key predictor of delays. Projects in the pre-FID stage had a zero success rate. However, even projects with an FID or under construction rarely met their schedules. Only 8% of announcements made in 2022 were delivered on time in 2023. Though delayed projects added capacity over time, the overall success rate was only 7%, corresponding to 0.3 GW of the originally announced 4.3 GW. The results differed in each region. Asia had above-average success, North America had average performance, and Europe had below-average success. These results highlight the structural implementation gap in global green hydrogen deployment.[20] Moreover, the evolving geopolitical landscape further complicates forecasting.[22] Given this volatile and limited data foundation, setting clear and realistic technology targets remains challenging. Despite the complex, technology-specific interactions involved, one cross-cutting priority should guide all clean energy technologies: material efficiency.[1,5,23]

Material efficiency is a critical consideration for any system, yet it is often overlooked in most scenarios and policy frameworks.[1] This is particularly important for PEMWE systems, as they rely heavily on iridium. To address this issue, the concept of iridium-specific power density (Ir-PD) was introduced as a metric to evaluate the feasibility of achieving PEMWE deployment targets in relation to iridium availability.[11,24–27] However, it is important to note that this metric is not linked to greenhouse gas emissions. At this point, Ir-PD must be recognized as a standalone priority from a system perspective. The available state-of-the-art (SoA) data for the PEMWE system currently exhibits significant variability, which can be partly explained by variations in the testing framework[28–31] and the materials[9,32–34] used. According to Clapp et al., the SoA Ir-PD ranges from 0.34 to 2.0 mg_{Ir} W^{-1} (equivalent to t_{Ir} GW^{-1}) based on data from several governmental and intergovernmental bodies, as well as academic sources.[11] A detailed explanation of the Ir-PD determination is given in the supplemental information. Bender et al. also reported this large discrepancy, finding deviations of up to 600 mV at 1 A cm^{-2} across the literature for the same membrane material.[28] Therefore, the actual magnitude of the required technological progress remains unclear. Considering this uncertainty, several targets were formulated in the range of 0.1 to 0.04 mg_{Ir} W^{-1}.[11,24] However, it was also stated that iridium dissolution could limit the reduction in iridium loading to 0.2 mg_{Ir} cm^{-2} and 0.1 mg_{Ir} W^{-1}.[11]

Iridium dissolution undermines the long-term stability of PEMWE systems and remains an obstacle to achieving the ambitious durability targets projected for 2030 (3 A cm^{-2}: 1.6 μV h^{-1} or 0.12% 1,000 h^{-1}).[35–37] Therefore, a fundamental understanding of the underlying mechanisms, especially under realistic device-level conditions, is of the utmost importance.[33] Dissolution that occurs before oxygen evolution begins is primarily driven by the formation of unstable oxide or hydroxide intermediates.[38] These intermediates are sensitive to the applied electrochemical protocol and can be mitigated by applying protective potentials.[39] At oxygen evolution reaction (OER) relevant potentials, dissolution is governed by reaction kinetics and believed to proceed via intermediates common to the OER pathway. This ultimately leads to a steady-state dissolution regime.[38] Despite its relevance, the mechanistic understanding of iridium dissolution remains incomplete, particularly at the device level and in relation to operation.[33] Recent studies highlight the severity of this phenomenon.[40–42] Only 6% of the dissolved iridium was detected in the anode outlet stream, while up to 43% accumulated within the membrane, indicating substantial iridium redistribution.[43] Iridium particle migration into the membrane has been observed across various systems.[44,45] Stähler et al. reported direct iridium cluster growth leading to filament from the anode to the cathode, resulting in an internal short circuit across the membrane.[46] This was evidenced by electrochemical impedance spectroscopy (EIS) and oxygen flow monitoring in single-cell setups.[46] This directed cluster formation is most likely the final stage of iridium dissolution, followed by migration within the membrane.

The dissolution process is fundamentally driven by the reactivity of iridium during the OER. Activation of iridium-based catalysts for the OER involves deprotonation reactions that extend from the surface into the bulk. This is particularly true for amorphous and semicrystalline iridium oxides, which could facilitate the dissolution of iridium species.[47] However, while amorphous iridium-based catalysts generally exhibit higher intrinsic reactivity, they are often associated with reduced structural stability. Conversely, rutile-type iridium oxides are more stable under OER conditions, though they have lower catalytic activity.[48–50] Activation of iridium-based catalysts involves the reversible formation of reactive oxygen species, such as μ_2-O, which emerge under anodic conditions and persist into the OER regime where μ_1-O and μ_1-OH coexist. Their potential-dependent appearance and disappearance reflect dynamic surface restructuring processes

that are closely tied to charge accumulation.[51] Such surface transformations are central to understanding the link between activation, charge dynamics, and long-term catalyst stability. While such phenomena are fundamental to understanding iridium-based catalyst behavior, their direct observation under realistic device-level conditions remains challenging. This underscores the importance of empirically investigating practical operating scenarios, especially when iridium loadings are reduced. The impact of reduced iridium loadings on Ir-PD and durability remains insufficiently explored at the device level.[9]

In this context, we analyzed four commercially available catalysts with loadings ranging from 0.1 to 0.8 mg_{Ir} cm^{-2} to review the SoA and the magnitude of improvement required. We extended this analysis with extensive durability testing of the catalysts. Iridium loadings of 0.1, 0.2, and 0.8 mg_{Ir} cm^{-2} underwent 500 h of stress testing under static and dynamic operation. Repeated experiments were conducted to ensure reliability. The most promising candidates were then subjected to 1,000 h of testing. The total measurement time for all the datasets presented in this work was approximately 20,000 h. Postmortem analysis, including cross-sectional imaging and extended X-ray photoelectron spectroscopy (XPS) characterization, revealed structural changes within the catalyst layers. Based on the observed performance trends, we estimated the potential market share that PEMWE could capture by using commercially available catalysts alone. This estimate excluded concurrent advancements to other key components, such as the membrane or the porous transport layer (PTL).

RESULTS AND DISCUSSION

Assessment of the raw materials

The four commercially iridium-based catalysts were selected from three different suppliers: H2EL-45IrO-S60 and H2EL-IrO (both Heraeus), Elyst Ir75 0480 (Umicore), and Premion (Alfa Aesar). The catalyst powders were analyzed by laser diffraction to obtain the particle size distribution (PSD) presented in Figure S1. All values are provided in Table S1. All reported values represent volume-weighted particle sizes. Premion was measured twice using the same batch and once using an older batch, showing only minor differences between the two measurements. The mean particle size of this catalyst was 13.6 ± 6.3 μm, with a d90 value of 15.4 μm. This indicated that 90% of the particles (d90) were smaller than 15.4 μm. The mean particle diameter was observed to be the highest for H2EL-45IrO-S60 (14.6 ± 16.7 μm) with a d90 of 37.7 μm, followed by H2EL-IrO (13.1 ± 10.5 μm) with a d90 of 29.2 μm. These two samples also exhibited the largest interquartile ranges (IQRs; the middle 50% of the distribution), with values of 17.0 and 11.9 μm, respectively. The smallest mean particle size was found for Elyst Ir75 0480 at 4.8 ± 6.3 μm, with a d90 of 15.4 μm. However, the surface areas obtained by nitrogen physisorption were 29 m^2 g^{-1} for Premion and 28 m^2 g^{-1} for Elyst Ir75 0480. In contrast, the surface areas for the Heraeus catalysts were larger: 103 m^2 g^{-1} for H2EL-45IrO-S60 and 254 m^2 g^{-1} for H2EL-IrO. The preparation of the dispersion formulation included extensive homogenization by an ultrasonic horn to break down larger agglomerates. Interestingly, the mean agglomerate size obtained after the dispersion process was 1.71 ± 0.74 μm for Premion, which is very similar to the 1.74 ± 0.7 μm obtained for H2EL-45IrO-S60. It was not possible to measure the formulated dispersion with the same laser diffraction device used for the powders because light could not pass through the dark dispersion. Ultrasonic spectroscopy requires stable dispersions due to the longer measurement time required. On the other hand, the H2EL-IrO formulation required different solvent mixtures and dilution than the other three catalysts. The resulting dilution caused the solid concentration to be too low for the ultrasonic spectroscope's measurement range. This underscores that the challenges associated with the catalyst layer do not solely originate from the material itself. In-depth analysis related to the dispersion formulation is often underexplored or simply not included in many publications. In this study, we assume that the dispersion formulation and the methods used cannot reach agglomerate sizes below 1.7 μm. Therefore, we acknowledge that determining the optimal dispersion for four different catalysts while studying technology-related effects is challenging.

Catalyst properties influence not only dispersion formulation but also govern electrochemical activity and stability through their composition and crystal structure. Energy-dispersive X-ray spectroscopy (EDX) coupled with SEM confirmed compositions within the specified ranges. Iridium loadings were calculated using the suppliers' nominal values. The catalyst stoichiometry was analyzed by temperature-programmed reduction (TPR). Following Peifer et al., the iridium oxidation state was derived for each catalyst.[52] For rutile-type IrO_2 (Ir^{+IV}), a theoretical H_2 consumption of 8.92 mmol g^{-1} is expected, whereas Ir_2O_3 (Ir^{+III}) corresponds to 6.94 mmol g^{-1}. Within these boundary cases, the average oxidation state of Premion was 3.5, with a maximum at 90.6°C. The determined oxidation state of H2EL-45IrO-S60 was 3.1, with a maximum at 95.9°C. These results indicated that both catalysts possess highly amorphous characteristics. In contrast, H2EL-IrO possessed an oxidation state of 3.9 and a maximum reduction temperature of 172.9°C, characteristic of a more rutile-like structure. The commercial Elyst-Ir75-0480 catalyst exhibited the highest average oxidation state of 4.0 and a relatively broad temperature window (120.9°C–247.8°C), also indicating a strong rutile-type nature. X-ray diffraction (XRD) patterns (Figure 1A) revealed unique structural features of each catalyst. Premion showed distinct metallic Ir peaks alongside a broad oxide reflection. Elyst Ir75 0480 and H2EL-IrO both exhibited broad oxide peaks characteristic of nanostructured iridium oxides, with Elyst Ir75 0480 showing slightly sharper reflections. H2EL-45IrO-S60 displayed only a single broad oxide peak. To clarify crystallinity versus amorphous contributions, XPS analysis was performed. Following Roiron et al., the Ir^{+III}/Ir^{+IV} ratio and μ_1-O/μ_2-O ratio were used to classify crystalline versus amorphous catalysts.[49] Figure 1B revealed the same trend of a more pronounced rutile-type nature: Elyst Ir75 0480 > H2EL-IrO > Premion > H2EL-45IrO-S60 as observed in the TPR measurements. This trend was also consistent with μ_1-O/μ_2-O ratios (Figure 1C) for three of the four catalysts.

From powder analysis, we concluded that H2EL-45IrO-S60 is an amorphous iridium oxide on titanium support, Premion

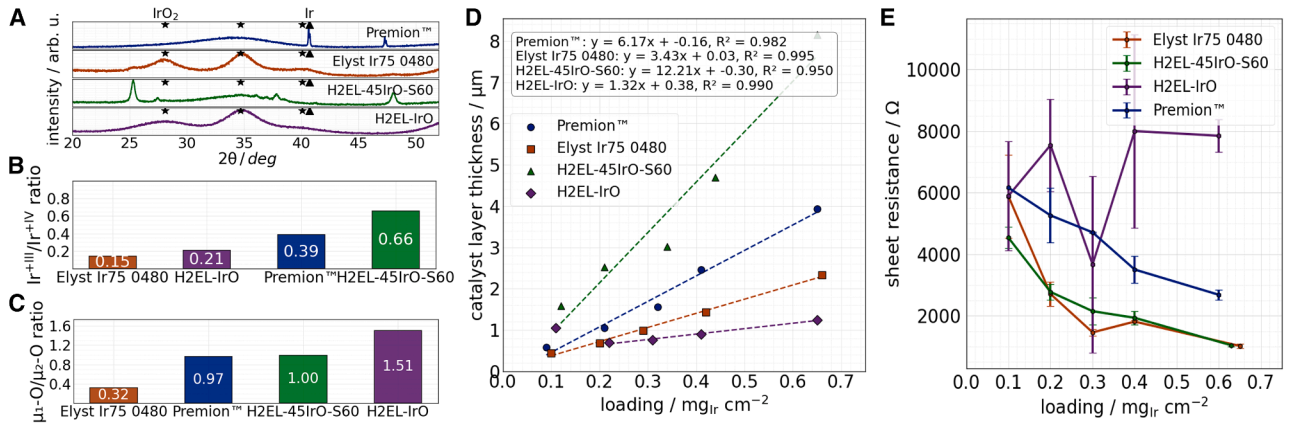

Figure 1. Physicochemical characterization of commercial iridium catalysts and pristine catalyst layers

Overview of the characterization conducted on the catalyst powders (A–C) and the pristine catalyst layers (D and E). The XRD patterns are shown in (A), where star and triangle symbols indicate the peak positions of iridium metal and iridium oxide, respectively. (B) displays the peak ratio of the Ir^{+III} and Ir^{+IV} species, and (C) displays the ratio between μ_1-O and μ_2-O surface oxygen functionalities. In (D), the catalyst-layer thickness obtained from image processing is displayed as a function of the respective loading. In (E), the same is presented for the sheet resistance. Error bars represent the standard deviation across independently prepared samples.

consists of an amorphous iridium oxide shell surrounding a metallic Ir core, H2EL-IrO is a rutile-type iridium oxide, and Elyst Ir75 0480 is a rutile-type iridium oxide on Ti support. Based on these assignments, the expected activity trend was H2EL-45IrO-S60 > Premion > H2EL-IrO > Elyst Ir75 0480, while the stability trend should follow the inverse order.

Prior to electrochemical testing, pristine catalyst layers were analyzed regarding the thickness (Figure 1D) and sheet resistance (Figure 1E). The catalyst-layer thickness was determined using a modification of a previously published method (details are provided in the supplemental information). Each catalyst exhibited a distinct thickness-loading relationship. Across all catalysts, the maximum difference between the lowest and highest layer thicknesses was 7.7 μm at the highest loading. Elyst Ir75 0480 and Premion had the lowest IQR: 0.1 mg_{Ir} cm^{-2}. The lowest absolute IQRs were obtained with lower loadings. However, compared to the average for these loadings, the relative IQR was greater than 40%. Outlier data points were excluded from the final analysis; however, their potential influence on durability cannot be entirely ruled out. For H2EL-IrO, thickness deviated from linearity at low loadings (<0.1 mg_{Ir} cm^{-2}), indicating insufficient film formation and possible island growth, resulting in locally thicker regions. In contrast, Elyst Ir75 0480 exhibited the lowest thickness at low loadings and consistently narrow IQRs. The absolute standard deviation increased with loading, whereas the relative deviation decreased. Linear regression yielded $R^2 > 0.98$ for all catalysts except H2EL-IrO, where strong scattering at <0.1 mg_{Ir} cm^{-2} reduced linearity, indicating that the PSD was more heterogeneous than for the other catalysts. Therefore, the linear fit excluded the lowest-loading data point for H2EL-IrO, resulting in an R^2 of 0.99.

The slope in Figure 1D reflects thickness sensitivity to loading. H2EL-45IrO-S60 showed the steepest slope, reflecting its composition and the greater volume required to achieve targeted loadings. Effective catalyst-layer density, defined as a reciprocal slope, was lowest for H2EL-45IrO-S60 (0.079 g_{Ir} cm^{-3}), compared with 0.24 g_{Ir} cm^{-3} for Elyst Ir75 0480 and 0.27 g_{Ir} cm^{-3} for Premion. For H2EL-IrO, the effective density was 1.01 g_{Ir} cm^{-3}. The non-zero intercept in the linear thickness-loading relationship arises from practical limitations in catalyst-layer fabrication and thickness determination at very low loadings. Residual contributions from ionomer distribution, substrate roughness, and coating inhomogeneities become increasingly relevant in the sub-micrometer thickness regime. Additionally, image resolution and pixel size at the required magnification for full catalyst-layer analysis limit the precise measurement of extremely thin catalyst layers. Therefore, the observed intercept reflects practical measurement and fabrication constraints rather than a theoretical zero-thickness condition. The sheet resistance was determined and correlated with both catalyst loading and average layer thickness. A significant decrease in sheet resistance with increasing loading or thickness was observed for all catalysts except H2EL-IrO. The inhomogeneous nature of the H2EL-IrO catalyst layer is also reflected in the wide variation of its sheet resistance values. Interestingly, the 0.1 mg_{Ir} cm^{-2} loading exhibited the highest measurement error in sheet resistance for all catalysts except H2EL-45IrO-S60. At the highest loading, Elyst Ir75 0480 and H2EL-45IrO-S60 showed similar sheet resistance values, although Elyst Ir75 0480 showed a steeper increase in resistance at lower loadings. The sheet resistance was normalized by the corresponding mean catalyst-layer thickness to obtain the in-plane electrical resistivity of each catalyst layer, enabling a thickness-independent comparison of the intrinsic electronic transport properties across catalysts and loadings. The resulting resistivity values revealed distinct, material-specific behavior that was largely independent of iridium loading and is shown in Figure S2. Elyst Ir75 0480 exhibited the lowest and most consistent resistivity across all loadings, ranging from 1.4 to 3.1 mΩ cm. H2EL-45IrO-S60 showed systematically higher resistivity values between 6.7 and 9.4 mΩ cm with no clear loading dependence, reflecting its highly porous,

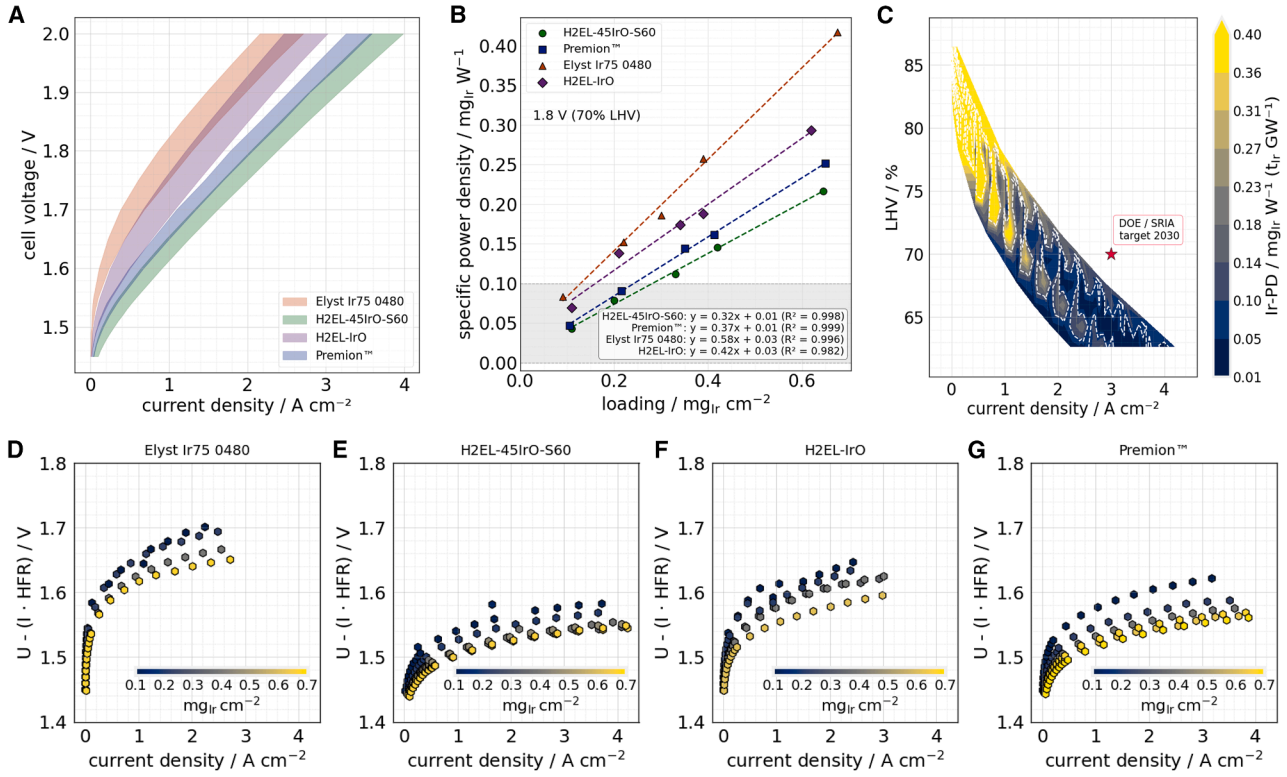

Figure 2. Performance screening results and iridium-specific power density of commercial iridium catalysts

Results of the performance screening are shown in (A), highlighting the performance range as a function of catalyst loading (0.1–0.7 mg_{Ir} cm^{-2}), and in (B), which displays the corresponding Ir-specific power density (Ir-PD) at 1.8 V. The visualization in (C) connects key performance metrics, including LHV, current density, and Ir-PD, to emphasize the importance of the system's operational window. HFR-corrected polarization curves for each catalyst and loading level are presented in (D)–(G).

titanium-supported character and correspondingly low effective catalyst density (see Figure 1D). Premion displayed intermediate, moderately increasing resistivity with loading, ranging from 3.6 to 6.7 mΩ cm. H2EL-IrO exhibited the most pronounced loading dependence, with resistivity increasing from 5.0 mΩ cm at 0.1 mg_{Ir} cm^{-2} to 17 mΩ cm at 0.7 mg_{Ir} cm^{-2}, which is attributed to the poor layer uniformity and island growth behavior identified in the thickness distribution analysis. Taken together, the thickness-normalized resistivity confirms that electronic transport properties are governed primarily by catalyst structure and morphology rather than by loading and that the observed differences in sheet resistance across loadings largely reflect variations in layer thickness rather than intrinsic material conductivity. Sheet resistance measurements were not performed after durability testing because the membrane and catalyst-layer structure underwent significant mechanical and structural alterations during operation and disassembly. Since water acts as a plasticizer for the Nafion membrane,[53] postmortem measurements would introduce substantial uncertainty and limit direct comparability to pristine-state values.

Performance screening

Initial performance was determined after the conditioning procedure for each catalyst and loading, with at least two repetitions. For easier comparison (Figure 2A), the area between the polarization curves of the lowest loading (0.1 mg_{Ir} cm^{-2}) and the highest loading (ca. 0.7 mg_{Ir} cm^{-2}) was shaded for each catalyst. All other curves fell within these limits. The polarization curves (Figure 2A) consistently reflected the catalytic activity trend identified in the Ir^{+III}/Ir^{+IV} ratio from XPS analysis (Figure 1B). At high loadings, the amorphous H2EL-45IrO-S60 achieved the highest current density with 2.4 ± 0.1 A cm^{-2} at 1.8 V, followed by Premion with 2.1 ± 0.1 A cm^{-2}. The rutile-type H2EL-IrO reached 1.7 ± 0.1 A cm^{-2}, while Elyst Ir75 0480 showed the lowest performance with 1.3 ± 0.1 A cm^{-2}. The corresponding average loading across all catalysts was 0.65 ± 0.02 mg_{Ir} cm^{-2} and equal to 3% variability. Notably, current density losses upon reducing the loading were smaller for Premion (−0.28 A cm^{-2} at 1.8 V) and H2EL-45IrO-S60 (−0.34 A cm^{-2}) but larger for Elyst Ir75 0480 (−0.43 A cm^{-2}) and H2EL-IrO (−0.48 A cm^{-2}) when the loading was reduced by 0.54 ± 0.03 mg_{Ir} cm^{-2}. Thus, the amorphous catalysts lost ca. 15% of performance, while the rutile-type catalysts lost ca. 35%. Two general trends were observed when studying the impact of the iridium loading reduction. The current density losses increased with cell voltage, and increased losses occurred when reducing the loading below 0.4 mg_{Ir} cm^{-2}, with an additional threshold at <0.3 mg_{Ir} cm^{-2}.

Analyzing the Ir-PD showed that all catalysts could reach the targeted 0.1 mg_{Ir} W^{-1} at 1.8 V (Figure 2B). However, when using

a thick N115 membrane together with a standard PTL, this target was only achieved with a loading of 0.2 mg_{Ir} cm^{-2} for the amorphous catalysts and with 0.1 mg_{Ir} cm^{-2} for the rutile-type catalysts. The threshold of 0.05 mg_{Ir} W^{-1} was only reached by the more amorphous catalyst types when using a loading of 0.1 mg_{Ir} cm^{-2}. Importantly, Ir-PD decreased linearly with loading ($R^2 > 0.99$) for all catalysts. An often overlooked factor is that Ir-PD targets are not linked to either stability or cell efficiency. Figure 2C reflects this SoA relationship by correlating the Ir-PD with the energy efficiency referenced to the lower heating value (LHV), plotted as a function of current density and based on the complete dataset.

The contour plot, constructed via Delaunay triangulation, highlights areas with Ir-PD below 0.1 mg_{Ir} W^{-1}, or the equivalent 0.1 t_{Ir} GW^{-1}, in blue and between >0.1 and <0.31 mg_{Ir} W^{-1} in gray. The identified threshold of 0.4 mg_{Ir} cm^{-2} is marked with a white dashed line. It becomes clear that the 0.1 mg_{Ir} W^{-1} target cannot be met at high efficiency levels >75% by catalyst design alone. Achieving such efficiencies with reduced iridium loading will require improvements in membranes, PTLs, and cell/stack assembly to reduce ohmic loss as much as possible. At lower efficiencies (<70%), the Ir-PD target is already close to being achieved for all catalysts. At 63% LHV (2 V) and 0.4 mg_{Ir} cm^{-2}, all catalysts reached the 0.1 mg_{Ir} W^{-1} threshold. This further implies that the 2030 DOE and SRIA target of 3 A cm^{-2} at 70% LHV cannot be met by catalyst design alone. Nonetheless, it is noteworthy that our results show that all commercial catalysts tested achieved an Ir-PD of $\leq$0.12 mg_{Ir} W^{-1} at 2 V with loadings of 0.65 ± 0.02 mg_{Ir} cm^{-2} in their initial stages.

The obtained polarization curves were normalized by high-frequency resistance (HFR) correction. This showed clearly that the rutile-type catalysts (Elyst Ir75 0480, H2EL-IrO) suffered from a higher activation overpotential than the more amorphous catalysts (Premion and H2EL-45IrO-S60). At a loading of 0.4 mg_{Ir} cm^{-2} and 1.8 V, the activation overpotential was 420 ± 47 mV for both rutile catalysts, while it was 373 ± 9 mV for H2EL-45IrO-S60 and 386 ± 5 mV for Premion. Reducing the loading to 0.1 mg_{Ir} cm^{-2} increased the activation overpotential by 36 mV for Elyst Ir75 0480, 22 mV for H2EL-IrO, 39 mV for H2EL-45IrO-S60, and 40 mV for Premion. This was reflected in the charge-transfer resistance (R_{ct}), or more neutral, in the diameter of the Nyquist semicircle. At the device level, R_{ct} represents the barrier that the charge must overcome to be transferred across the interfaces. Rct is strongly influenced by the effective contact area between the PTL and catalyst layer. This implies that the quality of the electrical contact depends on the thickness homogeneity and on the conductivity of the catalyst layer.

The sheet resistance measurements indicate that the anode catalyst layer itself represents a significant electronic resistance barrier, particularly at low iridium loadings. This suggests that electron transport through the catalyst layer can substantially influence local reaction distribution, favoring regions with shorter electronic pathways, such as areas directly below PTL contact points. With increasing current density, however, the reaction zone is additionally influenced by proton transport and mass transport limitations, which may increasingly shift active regions toward the membrane interface.

Analyzing R_{ct} at 1.45 V (Figure S3A) for the different catalysts and loadings revealed an inverse logarithmic relationship between the applied iridium loading and the resulting R_{ct}.

Although R_{ct} increased most strongly for the rutile catalysts and remained comparatively lower for the amorphous ones. These differences likely arise from a combination of factors, including activity differences between rutile-type and amorphous iridium oxides; variations in coating thickness ranged from less than 1 μm to greater than 2.5 μm near the onset of the steep R_{ct} increase and increased sheet resistances with decreased loading for all catalysts. Thus, the R_{ct} trends likely reflect an interplay of iridium dispersity, coating uniformity, sheet resistance, and catalyst-layer thickness rather than a single dominant effect. Between the two titanium-supported catalysts, one order of magnitude difference was observed at 0.4 mg_{Ir} cm^{-2} with 0.49 ± 0.15 mΩ cm^2 for H2EL-45IrO-S60 and 5.75 ± 0.69 mΩ cm^2 for Elyst Ir75 0480. At 0.1 mg_{Ir} cm^{-2}, R_{ct} increased to 1.71 ± 0.63 and 16.0 ± 2.92 mΩ cm^2, respectively. Remarkably, R_{ct} increased steeply for all catalysts with 0.1 mg_{Ir} cm^{-2}. On the other hand, R_{ct} for the amorphous catalysts was not affected by increased loading. This indicated that in a typical high-loaded CCM, a certain fraction of the catalyst remains inactive.

The HFR analysis was more challenging and is presented in Figure S3B. The performance screening with repetitions required more than 50 single-cell tests, which involved multiple membranes, cathode catalyst layers, and PTLs, all contributing to HFR variability. Especially at low loadings, PTLs showed visible changes after repeated use, which required the exchange of components from time to time. On average, HFR across all measurements was 123 ± 13.2 mΩ cm^2 at 1.45 V. Each catalyst showed a distinct HFR behavior with no clear correlation to the sheet resistance. H2EL-45IrO-S60 showed a clear HFR increase with decreasing iridium loading, while Elyst Ir75 0480 showed an increase in HFR with higher loadings. However, the dominant contribution to HFR originated from the membrane, which obscured a clear assessment of the effect of loading reduction and corresponding sheet resistance on HFR.

Durability testing of low loadings

The 500 h durability test was conducted for all catalysts at loadings of 0.4, 0.2, and 0.1 mg_{Ir} cm^{-2}. In each case, five tests were performed simultaneously using an in-house-built multichannel test station, with one test always using the Premion catalyst at 0.8 mg_{Ir} cm^{-2} as a benchmark. Variability in the dataset originated mainly from the PTL, as each test required a different PTL. Furthermore, the durability tests were performed with a different temperature control system than the one used for performance screening. Performance screening used water inlet temperature as the control parameter to ensure the temperature difference between the inlet and outlet remained within ±2°C. In contrast, the durability tests were carried out with temperature regulation recorded directly at the single-cell endplates. For this reason, the durability data are compared only within their own dataset and not with the performance screening results. To confirm consistency, durability tests were repeated for selected candidates. The difference between the averaged benchmark measurements recorded during the performance

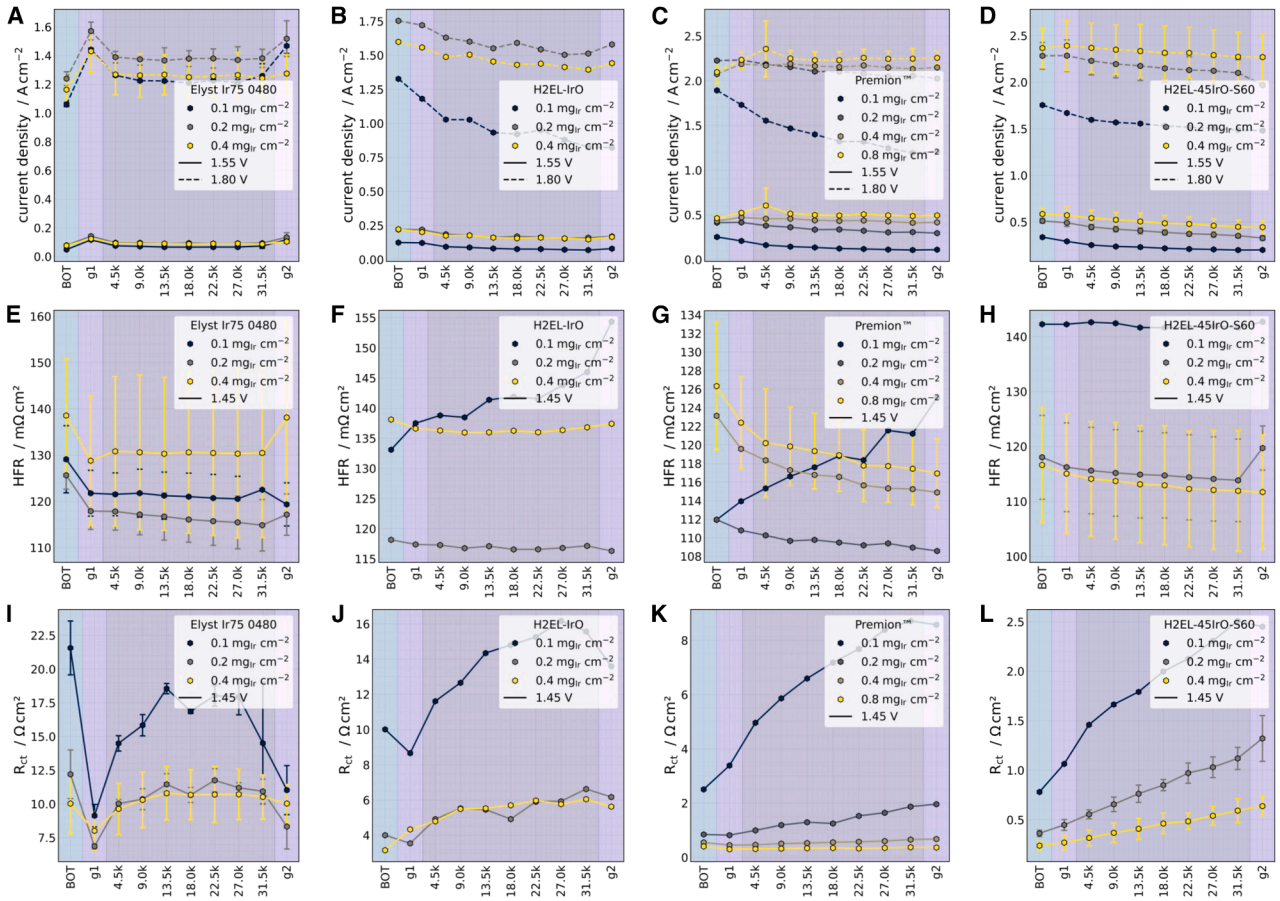

Figure 3. Durability testing results for all investigated commercial iridium catalysts and loadings

Results from the durability testing are shown in (A)–(L): current density is presented in (A–D), high-frequency resistance (HFR) in (E–H), and charge-transfer resistance (R_{ct}) in (I–L). The data for each catalyst are displayed according to their TPR/XPS classification, ranging from rutile to more amorphous characteristics: Elyst Ir74 0480 in (A, E, and I); H2EL-IrO in (B, F, and J); Premion in (C, G, and K); and H2EL-45IrO-S60 in (D, H, and L). Error bars represent the standard deviation across repeated tests of the same catalyst and loading, each conducted with new PTLs and membranes.

characterization and the beginning of testing (BOT) of the durability testing was 120 mA cm^{-2} at 1.8 V. This offset is inherent to the two test stations because it was determined using an identical benchmark configuration on both systems.

In each plot of Figure 3, the BOT is indicated, followed by the first galvanostatic phase (g1) at 2 A cm^{-2} for 100 h. After g1, seven 4,500 triangle cycles were performed, after which the test ended with another galvanostatic phase (g2) at 2 A cm^{-2} for 100 h. Figures 3A–3D show the current density extracted from the polarization curves for each catalyst at a cell voltage of 1.55 V as a solid line and at 1.80 V as a dashed line. The second row (Figures 3E–3H) shows the determined HFR at 1.45 V, and the extracted R_{ct} at 1.45 V is shown in the third row (Figures 3I–3L).

The Elyst Ir75 0480 (Figures 3A–3E and 3I) catalyst exhibited increased current density (+286 ± 174 mA cm^{-2} at 0.4 mg_{Ir} cm^{-2}|1.8 V) after g1. This increase also occurred after g2 at the end of testing, though it was less pronounced (+32.7 ± 197 mA cm^{-2} at 0.4 mg_{Ir} cm^{-2}) than the current density recorded after 31,500 cycles. The observed initial performance increase in Elyst Ir75 0480 may indicate an activation process during early operation. Potentially, less stable amorphous or defective surface species arising from catalyst batch impurities or structural heterogeneities may be altered or removed during initial operation. This could improve catalyst accessibility, interfacial contact, or charge-transfer properties. A strong decay was observed for all loadings of H2EL-IrO. The Premion benchmark catalyst, with a loading of 0.8 mg_{Ir} cm^{-2}, improved by 7% over time, while the 0.4 mg_{Ir} cm^{-2} loading improved by 4%. The loadings of 0.2 and 0.1 mg_{Ir} cm^{-2} decreased by 10% and 56%, respectively. This effect also occurred for lower loadings, but not for any of the other catalysts. The amorphous H2EL-45IrO-S60 (Figure 3D) exhibited a 9.6% current density loss at 0.4 mg_{Ir} cm^{-2} between BOT and g2, whereas the current density decreased by 16% at 0.1 mg_{Ir} cm^{-2}.

The determined HFR (Figures 3E–3H) decreased steadily for certain catalysts and loadings. The HFR decreased by 8% and 7% for 0.1 and 0.2 mg_{Ir} cm^{-2}, respectively, during the entire test for Elyst Ir75 0480. The HFR also decreased for 0.4 mg_{Ir} cm^{-2} H2EL-45IrO-S60 and Premion loadings $\geq$ 0.2 mg_{Ir} cm^{-2}.

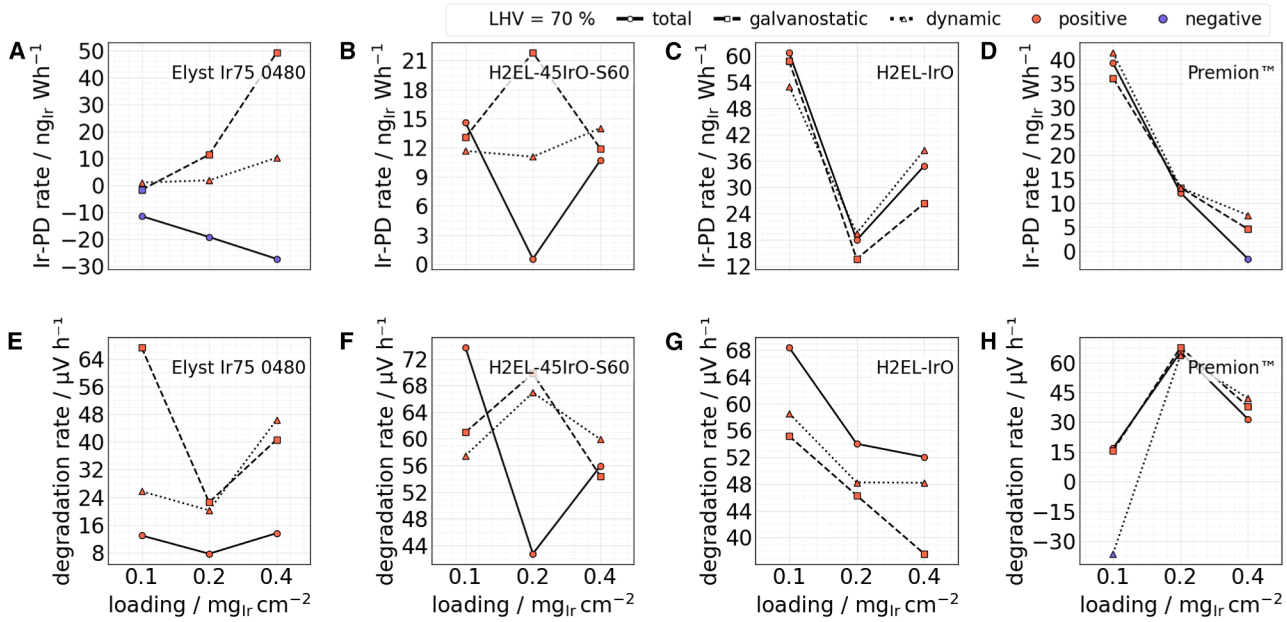

Figure 4. Degradation rates extracted from HFR-corrected polarization curve data

In (A)–(D), the change in Ir-PD is displayed, and in (E)–(H), the degradation rate is shown for all catalysts and loadings stress tested for 500 h: the total degradation rate (circles), the rate during the dynamic stress phase (triangles), and the rate between both galvanostatic phases (squares).

One potential reason is that membrane creep leads to thinner membrane compartments, which decreases the HFR. However, the HFR increased by more than 10% for 0.1 $mg_{Ir}\,cm^{-2}$ loadings (H2EL-IrO and Premion). This could be due to an altered interface with the PTL or membrane poisoning by dissolution products from the PTL or the catalyst itself. Conversely, the decreased HFR masks the current density loss at voltages > 1.8 V, making it appear as an improved overall cell performance at higher cell voltages. Recent studies by Hintzen et al. have shown that membrane creep, PTL compression, and local contact-pressure distributions can significantly influence membrane thickness evolution and HFR behavior in PEMWE systems.[54] Although SEM cross-sections provided important structural insights into catalyst-layer evolution, this study did not pursue direct quantification of absolute membrane thickness changes from these images. Quantitative membrane creep analysis requires a methodology that accounts for strong couplings among mechanical, structural, and operational factors, including PTL compression, local contact-pressure distributions, membrane swelling, flow-field-specific channel-rib geometry, and postmortem preparation artifacts. This methodology lies beyond the scope of this work.

Therefore, HFR-related changes in this study were interpreted cautiously, while HFR-corrected polarization curves and R_{ct} analysis were used as the primary metrics to minimize broader system-level effects and enable more catalyst-specific evaluation. In the kinetic region, stronger catalyst alteration was observed, which aligned well with the determined R_{ct}.

The R_{ct} (Figures 3I–3L) increased linearly for all catalysts and loadings, except for Elyst Ir75 0480. The observed change indicates an alteration either at the catalyst interfaces or within the ionomer network. However, the striking linear increase was not affected by either galvanostatic or dynamic phases. This implies that another ongoing degradation process occurred that is not solely dependent on electrochemistry. We consider temperature to be an underexplored driving force in the degradation effect owing to its correlation with iridium and titanium dissolution. Another interesting point is that the rutile Elyst Ir75 0480 behaved completely differently. Surprisingly, the galvanostatic phases lowered the R_{ct}, which disappeared after dynamic testing. Instead, the dynamic phases did not significantly affect the R_{ct} during testing. One potential explanation is that during galvanostatic operation, kinetics and quasi-equilibria lead to the reorganization of defective species in the lattice based on place-exchange events.[38] Progressive catalyst utilization losses may contribute to the observed linear R_{ct} increase, as reduced active-site accessibility or interfacial degradation directly affects kinetic performance. While changes in HFR may partially reflect broader structural or contact alterations, the dominant R_{ct} evolution suggests that utilization-related losses are primarily associated with catalyst-layer or ionomer-network degradation rather than purely ohmic effects.

Degradation rates were determined to compare the different catalysts. In Figure 4, the change in Ir-PD (top row, Figures 4A–4D) and the degradation rate (bottom row, Figures 4E–4I), extracted from HFR-corrected polarization curves, are presented at 1.8 V or approximately 70% LHV. All degradation rates were determined by linear fitting of the HFR-corrected performance data obtained from the polarization curves over the respective evaluation period. Separate fits were applied to the complete dataset (BoL to EoL), the dynamic stress phase, and the interval between both galvanostatic phases to isolate the corresponding operational contributions. Accordingly, Figure 4 presents the total evolution rate between

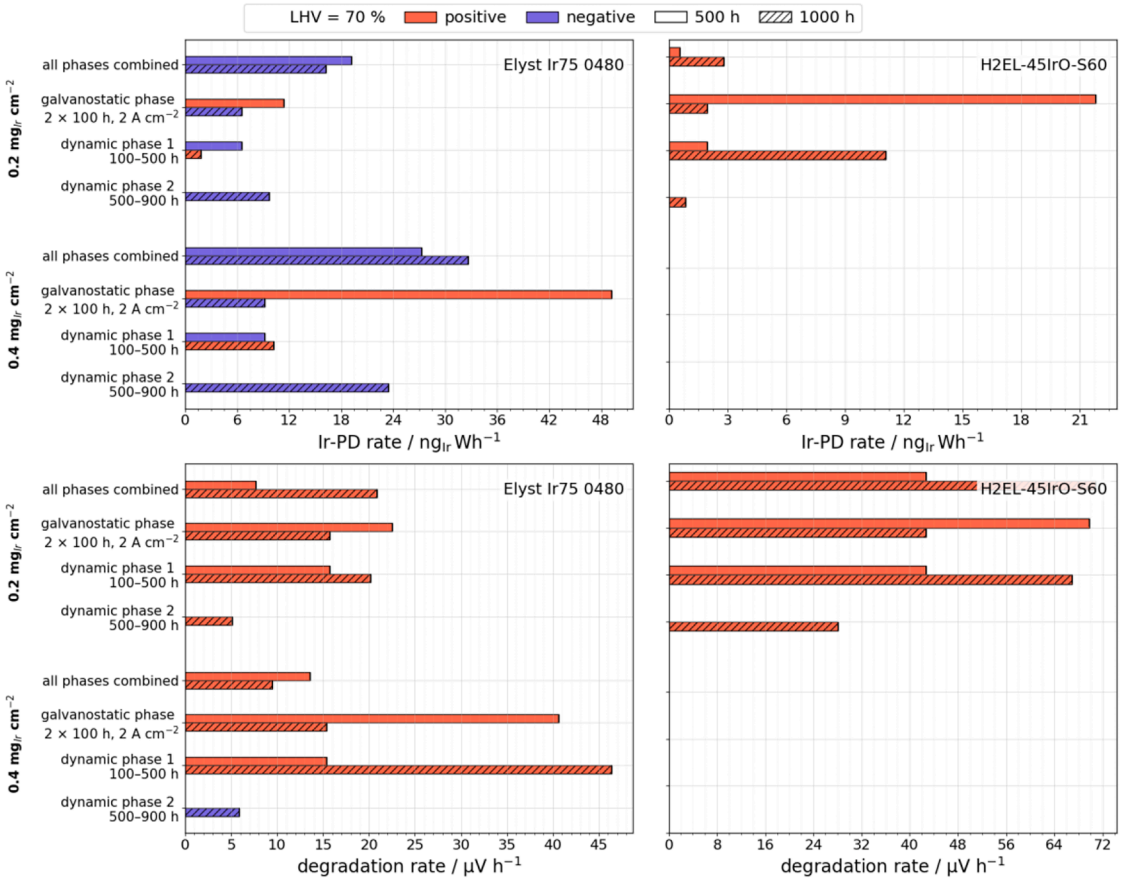

Figure 5. Degradation rates extracted from HFR-corrected polarization curve data for Elyst Ir75 0480 and H2EL-45IrO-S60 over 500 and 1,000 h stress tests

Shown are the changes in Ir-specific power density (Ir-PD) and degradation rates for total, galvanostatic, and dynamic operating phases across selected catalyst loadings, enabling direct comparison of loading-, catalyst-, and operation-dependent durability behavior. The underlying HFR-corrected data are provided in Figure S5.

BoL and EoL (circles), the rate during the dynamic stress phase (triangles), and the rate between both galvanostatic phases (squares). The change in the Ir-PD rate can be interpreted as catalyst efficiency over time. An increase or decrease indicates a gain or loss in material efficiency during operation. The maximum observed Ir-PD rate was <70 $ng_{Ir}\,Wh^{-1}$, and most catalysts and loadings exhibited an increased Ir-PD rate. This suggests that catalyst utilization decreased due to dissolution or structural changes affecting kinetics. Overall, dynamic testing caused more significant alterations than galvanostatic testing. Although no universal trend was identified across all catalysts and loadings, each system displayed distinct behavior. The complex interplay among cell compression, catalyst-layer thickness, membrane properties, temperature, hot-zone formation, and additional component interactions can cause each specific component combination to exhibit distinct degradation behavior and corresponding degradation rates, complicating the identification of universal degradation trends.

The most significant degradation was found for H2EL-IrO, as indicated by both variables. Theoretically, this rutile-classified catalyst should be more stable than amorphous catalysts. However, lower catalyst-layer quality, suggested by thickness and sheet resistance analysis, may explain the discrepancy. This underlines the need for further research to better understand catalyst integration.

The lowest degradation rates were determined for the rutile Elyst Ir75 0480. Interestingly, the highest iridium loading did not always result in the lowest degradation rate during dynamic testing.

For the 1,000 h durability testing, Elyst Ir75 0480 and H2EL-45IrO-S60 were selected as the most promising candidates for extended evaluation. The selected loadings included two tests at 0.4 $mg_{Ir}\,cm^{-2}$ and one at 0.2 $mg_{Ir}\,cm^{-2}$ for Elyst Ir75 0480, while two tests at 0.2 $mg_{Ir}\,cm^{-2}$ were performed for H2EL-45IrO-S60 (Figure S3). The 0.4 $mg_{Ir}\,cm^{-2}$ condition for H2EL-45IrO-S60 was not included in the extended 1,000 h testing due to resource constraints, which limits direct loading-resolved comparison with Elyst Ir75 0480 at this loading in Figure 5. At present, a trade-off appears to exist between a highly active but strongly changing amorphous catalyst and a less active yet more stable rutile-based catalyst. If titanium-supported catalysts prove stable under operating conditions, they may offer a

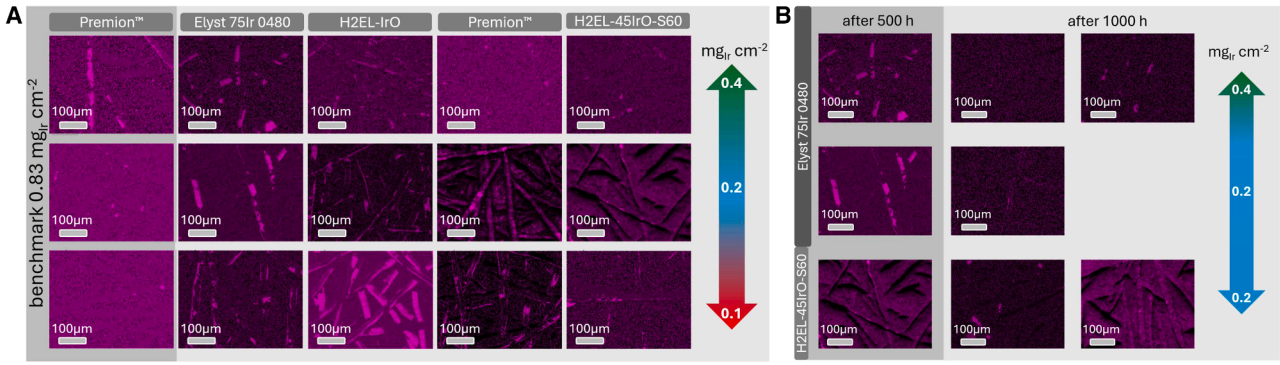

Figure 6. Platinum delamination from the PTL onto the catalyst layer observed after long-term durability testing

EDX measurements coupled with SEM analysis showed delamination of the platinum coating from the PTL onto the catalyst layer after 500 (A) and 1,000 (B) h of operation.

meaningful improvement over existing single-metal oxide catalysts. The 0.2 mg_{Ir} cm^{-2} loading already appears to be a limiting value due to dissolution effects.[11] On the other hand, our initial performance screening suggested that low loadings of 0.1 mg_{Ir} cm^{-2} may no longer be necessary in the future, thanks to advancements in other components required to meet the DOE target of 3 A cm^{-2} at 1.8 V. Observations during the 1,000 h test mirrored previous findings. At 1.8 V, the current density increased for Elyst Ir75 0480 by 374 and 308 mA cm^{-2} for 0.2 and 0.4 mg_{Ir} cm^{-2}, respectively. In contrast, the current density decreased by 161 mA cm^{-2} (7%) for H2EL-45IrO-S60 at 0.2 mg_{Ir} cm^{-2}. However, in the kinetic region at 1.55 V, the current density loss was ca. 40% for the H2EL-45IrO-S60 and improved by more than 20% for the Elyst Ir75 0480. The HFR decreased consistently for both catalysts, by approximately 26% on average for Elyst Ir75 0480 (Figure S4B) and by 11% for H2EL-45IrO-S60 (Figure S4A). This implies ongoing membrane creep or thinning. However, the extent of creep may also depend on the catalyst layer thickness, which can act as a backing layer if sufficiently thick, as observed for H2EL-45Ir-S60. Additionally, improvements may have occurred at the PTL-catalyst layer interface. However, the R_{ct} increased almost linearly (Figure S4C) for H2EL-45IrO-S60, rising from 0.36 to 1.99 Ω cm^2, an increase by a factor of 5.5. Still, this value remained five times lower than that of Elyst Ir75 0480 (Figure S4D) at the same loading (0.2 mg_{Ir} cm^{-2}). For Elyst Ir75 0480, R_{ct} decreased by 18%, from 12 to 10 Ω cm^2 (0.2 mg_{Ir} cm^{-2}) and from 10 to 9.6 Ω cm^2. Therefore, the change in HFR must have another origin and is likely not predominantly affected by the catalyst itself, though this could shift when using thinner membranes. Analysis of extracted degradation rates highlighted a clear trend across, as shown in Figure 5. Regarding the Ir-PD rate, material efficiency improved, and it became clear that only the first dynamic phase led to a declining Ir-PD rate for Elyst Ir75 0480. In the 1,000 h durability test, the degradation rate for the 0.2 mg_{Ir} cm^{-2} loading of Elyst Ir75 0480 shifted from 20 µV h^{-1} in the first period to −5.1 µV h^{-1} in the second period. For H2EL-45IrO-S60 at 0.2 mg_{Ir} cm^{-2}, the degradation rate was reduced by more than half, from 67 to 28 µV h^{-1}. A similar trend was observed for the Ir-PD rate. The degradation rate determined from the galvanostatic phase also showed this trend and was reduced with extended durability testing. Analysis of the R^2 of the linear fit revealed values > 0.95 for H2EL-45IrO-S60 in both periods.

For Elyst Ir75 0480, R^2 was >0.82 in the first period but dropped to <0.2 in the second, possibly indicating a new steady-state condition. For H2EL-45IrO-S60, the degradation followed a pattern similar to the inverse logarithmic decay behavior commonly observed in many degradation processes. This would offer an interesting trade-off for future PEMWE systems. Either a less active but relatively stable catalyst or a more active but strongly changing amorphous catalyst can be chosen. The key question is which option causes fewer issues during its transition (e.g., leaching of Ti^{4+} or Ir^{3+}) and whether these effects can be mitigated to enable the use of highly active materials. If the degradation losses become less pronounced after the initial transition, the trade-off may favor catalysts with higher intrinsic activity, which become more crystalline during operation.

The hard-to-swallow pill is that research must now prioritize these aspects, aligning with the reality that resource-intensive testing capabilities will increasingly be occupied by long-term studies requiring testing durations of at least 1,000 h in the future. Accelerated stress tests currently function more as stress-inducing tests, as the data pool remains too limited to yield statistically meaningful results. In the coming decade, research should shift its focus toward reliability, the durability of integrated materials, and their interactions with other components rather than obsessively chasing peak performance metrics.

Postmortem analysis

In this study, SEM coupled with EDX was initially used to analyze the catalyst layer surface. In the EDX images in Figure 6, platinum is represented by magenta. This makes its presence and dispersion within the catalyst layer clearly distinguishable from the other elements. The magenta contrast highlights regions of higher local platinum intensity, revealing particle clusters, delaminated coatings, and traces on top of the catalyst layer. A relatively large amount of platinum was observed on the catalyst layer surface after 500 (Figure 6A) and 1,000 (Figure 6B) h. However, the benchmark CCM (Premion, ∼0.8 mg_{Ir} cm^{-2}) showed only a few isolated spots with platinum located on top of the

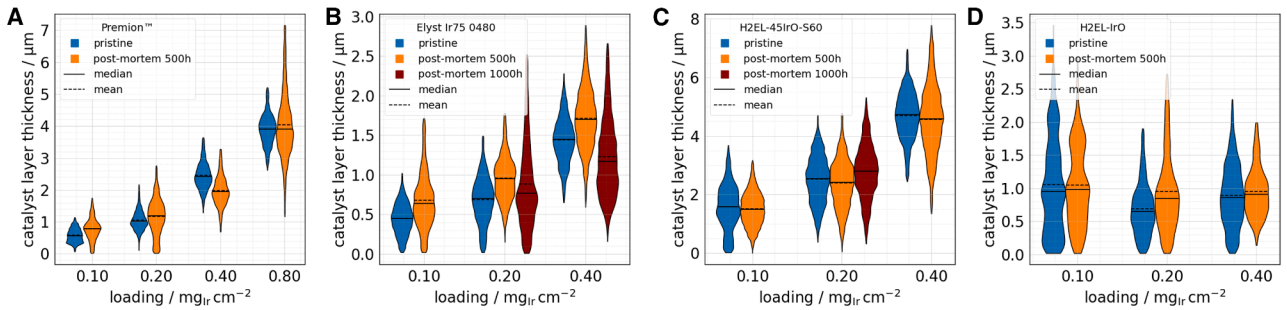

Figure 7. Thickness distributions obtained from image analysis for the different catalysts and loadings before and after durability testing. Panels show results for (A) Premion, (B) Elyst Ir75 0480, (C) H2EL-IrO, and (D) H2EL-45IrO-S60.

catalyst layer. In contrast, reduced iridium loading led to increased platinum deposition. Notably, rutile-type catalysts exhibited larger platinum accumulations on the surface.

In all cases, platinum was predominantly found in indented areas of the PTL. This suggests that dynamic operation affects the protective coating of the PTL, which remains stable under constant operating conditions. It remains unclear whether the coating delaminated from the PTL due to redeposition or whether it was delaminated during disassembly. If the latter is true, this would imply ongoing interaction between the platinum coating and the catalyst layer, increasing adhesion forces to the extent that the coating delaminated from the PTL onto the catalyst layer. This effect was especially pronounced for H2EL-IrO, which also exhibited the lowest catalyst layer quality. Therefore, the superacidity of Nafion, together with the membrane creep, may catalyze platinum migration from the protective coating toward the PTL by attacking exposed titanium oxide sites or platinum directly.

The degradation of the catalyst layers was evaluated by comparing pristine specimens with postmortem cross-sections after 500 and 1,000 h of durability testing. In Figure 7, the thickness distributions are presented as violin plots. For each loading, the layer thickness was determined before and after durability testing. The mean and median values are indicated by solid and dashed lines, respectively. Distinct trends in both mean thickness and distribution spread were observed, depending on catalyst type and loading. In some cases (e.g., H2EL-IrO), the difference between mean and median increased, indicating a stronger asymmetry in thickness distribution after operation. At low loading, Premion layers (Figure 7A) exhibited slight thickening, from 0.58 to 0.78 µm for 0.1 mg$_{Ir}$ cm^{-2} and from 1.05 to 1.17 µm for 0.2 mg$_{Ir}$ cm^{-2}, along with a noticeable increase in standard deviation (from 0.22 to 0.35 µm and from 0.31 to 0.57 µm, respectively). This suggests moderate structural thickening coupled with growing heterogeneity. At intermediate loading (0.4 mg$_{Ir}$ cm^{-2}), the mean thickness decreased from 2.46 to 1.97 µm, while the spread remained relatively constant. At high loading (0.8 mg$_{Ir}$ cm^{-2}), the mean increased slightly from 3.90 to 4.04 µm, but the distribution broadened considerably (standard deviation increased from 0.48 to 1.06 µm, with the maximum thickness reaching 7.16 µm). These results underscore Premion's structural changes, revealing loading-dependent degradation pathways: modest thickening at low loading, thinning at intermediate loading, and pronounced roughening at high loading.

Elyst Ir75 0480 (Figure 7B) showed a two-stage degradation pattern. At 0.1 mg$_{Ir}$ cm^{-2}, the mean thickness increased from 0.45 to 0.68 µm, with a modest rise in distribution spread. At 0.2 mg$_{Ir}$ cm^{-2}, the pristine layer thickness averaged 0.68 µm, increased to 0.96 µm after 500 h, and then slightly decreased to 0.88 µm after 1,000 h. The spread remained small after 500 h but increased after 1,000 h, suggesting growing structural heterogeneity over time. A similar trend was observed at 0.4 mg$_{Ir}$ cm^{-2}, where the mean rose from 1.44 to 1.71 µm at 500 h, then decreased to 1.23 µm at 1,000 h. The standard deviation increased steadily at a rate of approximately +0.1 µm per 500 h. Overall, the catalyst layers based on Elyst Ir75 0480 initially thickened, followed by a gradual reduction in mean thickness and a broadening of the thickness distribution during extended operation. H2EL-45IrO-S60 (Figure 7C) demonstrated the lowest change in thickness among all catalysts. At 0.1 mg$_{Ir}$ cm^{-2}, the mean thickness decreased only slightly from 1.58 to 1.52 µm, and the distribution even narrowed. Using 0.2 mg$_{Ir}$ cm^{-2}, pristine layers averaged 2.52 µm and changed only marginally, from 2.39 µm at 500 h to 2.79 µm at 1,000 h, with consistently narrow distributions. At 0.4 mg$_{Ir}$ cm^{-2}, the mean thickness decreased minimally from 4.70 to 4.57 µm after 500 h, indicating relatively low thickness changes.

H2EL-IrO (Figure 7D) exhibited the least favorable behavior. While mean thickness values changed only slightly, from 1.06 to 1.05 µm at 0.1 mg$_{Ir}$ cm^{-2}, from 0.69 to 0.95 µm at 0.2 mg$_{Ir}$ cm^{-2}, and from 0.89 to 0.95 µm at 0.4 mg$_{Ir}$ cm^{-2}, the standard deviation was consistently high. Even in the pristine state, the spread reached 0.72 µm at 0.1 mg$_{Ir}$ cm^{-2} and 0.40 µm at 0.2 mg$_{Ir}$ cm^{-2}, indicating poor initial layer uniformity. After 500 h, variability remained large or increased further, with wide interquartile ranges and maximum values up to 3.46 µm. This persistent heterogeneity suggests that the apparent stability in mean thickness masks underlying degradation and points to inferior layer quality compared to other formulations, most likely explaining the higher degradation rates observed during testing.

The overall trend across the dataset is an initial thickening within the first 500 h, followed by either a reduction in mean thickness or an increase in heterogeneity during extended operation. Premion displayed the greatest instability, with degradation behavior dependent on iridium loading. Elyst Ir75 0480

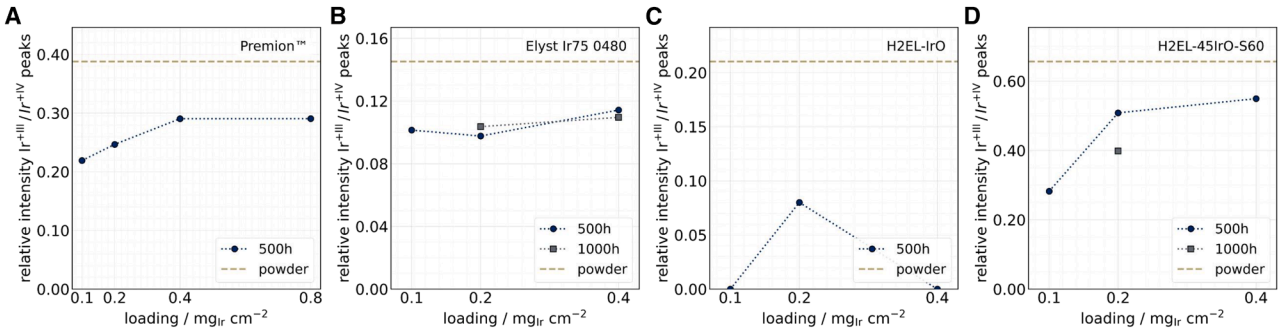

Figure 8. Postmortem XPS analysis showed characteristic differences between rutile and amorphous catalysts at various loadings
Shown for (A) Premion, (B) Elyst Ir75 0480, (C) H2EL-IrO, and (D) H2EL-45IrO-S60.

followed a two-stage progression involving early thickening and later thinning, while H2EL-45IrO-S60 remained stable with minimal changes. H2EL-IrO, in contrast, exhibited consistently high variability and poor layer integrity throughout.

Correlating these results with the findings from durability testing reveals that, whatever the catalyst, significant material relocation altered the structure of the catalyst layer. Dissolution-reprecipitation processes or agglomeration via Ostwald ripening may account for the broader data spread and increasing heterogeneity. Notably, each catalyst exhibited distinct, time-dependent degradation behavior during stress testing, supporting the conclusion that the most substantial changes occurred in the early phases of operation. This is consistent with degradation rate analysis. Furthermore, there may be a loading- or thickness-dependent degradation mechanism that remains poorly understood. Increased structural heterogeneity and broader thickness distributions after operation can additionally shift the arithmetic mean toward higher values, even when simultaneous local thinning occurs, which may partially contribute to the apparent thickening. Additional studies are needed to determine whether thickness changes occur locally at the PTL-catalyst layer interface or in regions not in contact with the PTL. The influence of the channel-land structure in the flow field and the effects of cell compression should also be further investigated.

XPS analysis was used to study the Ir^{+III}/Ir^{+IV} ratio. The oxygen spectrum was excluded from further evaluation due to the numerous challenges in interpreting and fitting data in the presence of Nafion-related oxygen functionalities. Figure 8 presents the Ir^{+III}/Ir^{+IV} ratio for each catalyst and studied loading after durability testing. The dashed line represents the Ir^{+III}/Ir^{+IV} obtained from powder analysis. In general, all binding energies were shifted by approximately +1 eV, regardless of whether platinum or iridium was being measured. Detected platinum appeared both as metallic and as PtO_2. When platinum was present in the XPS spectra, it affected the iridium envelope and baseline offset, introducing non-quantified uncertainties during fitting. All catalysts exhibited lower Ir^{+III}/Ir^{+IV} ratios after testing compared to their powder-state reference values, indicating that the catalysts crystallized during operation. For H2EL-IrO, analysis was not possible due to a low signal-to-noise ratio and insufficient spectral intensity. For Premion, no differences were observed at loadings $\geq$ 0.4 mg_{Ir} cm^{-2}. However, at loadings < 0.4 mg_{Ir} cm^{-2}, the Ir^{+III}/Ir^{+IV} ratio decreased with decreasing iridium loading, indicating increased crystallinity. This same trend was also observed for H2EL-45IrO-S60. Increased crystallinity, with reduced activity relative to the amorphous state, may explain the drop in current density in the kinetic region, which was consistent with the R_{ct} data. The observed increase in crystallinity strongly correlates with the previously discussed linear R_{ct} increase (Figures 3I–3L and S4), particularly for the more amorphous catalysts at reduced loadings. This suggests that catalyst crystallization and the associated loss of intrinsic activity are major contributors to the measured kinetic degradation. Crystallinity further increased after 1,000 h of testing for H2EL-45IrO-S60 at 0.4 mg_{Ir} cm^{-2}. In contrast, the rutile-type Elyst Ir75 0480 showed little to no change before and after testing, suggesting it already possessed a sufficient crystalline structure.

One question that remains is why higher loadings were not similarly affected. We postulate that this may be due to large, inactive catalyst compartments located at the catalyst layer surface. Depending on the location of the active reaction zone, such surface compartments may remain too far from the electrochemical reaction zone to experience significant potential, membrane acidity, hydrogen crossover, or voltage fluctuations. As a result, not all of the catalyst is altered during operation at high loading.

It is important to note that XPS signal intensity is influenced not only by the electron penetration depth but also by the area excited during measurement. This means the detected signal is inherently averaged over both depth and lateral spread, which could mask localized changes in catalyst structure.

XPS provided valuable insights that warrant further investigation in future studies. However, progress in this area is closely tied to the development of improved measurement procedures for analyzing catalyst layers on polymer substrates.[55] To address these challenges, future efforts should focus on standardizing methodologies and establishing robust measurement protocols for XPS-based analysis.

Recap and outlook

Reviewing the results of the performance and durability study highlights that commercial iridium catalysts are already capable of meeting near-future Ir-PD targets when paired with SoA components. However, considering the DOE target of 3 A cm^{-2} at

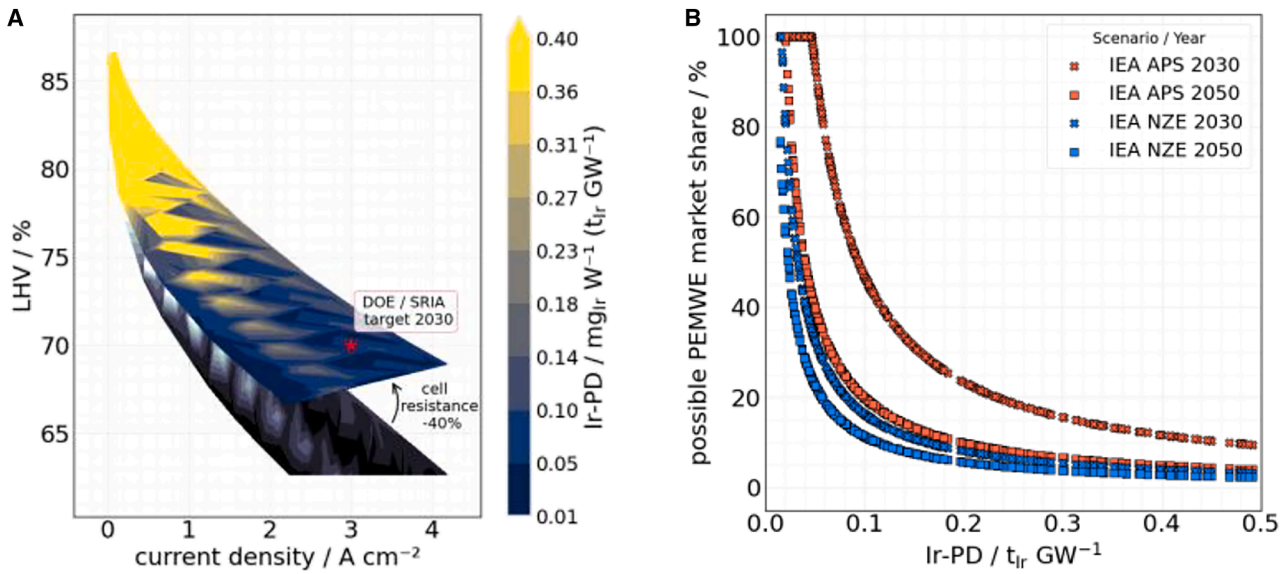

Figure 9. Impact of cell resistance reduction and iridium availability on feasible PEMWE deployment

To shift the perspective in the current discourse on iridium availability and criticality, a 40% reduction in cell resistance was modeled and its impact on Ir-PD analyzed (A). Additionally, the technically feasible PEMWE market share was estimated in (B) based on data obtained in this study, under the assumption of an annual iridium availability of 1.5 t.

1.8 V, it becomes evident that such performance cannot be achieved through catalyst design alone. To emphasize this, we modeled the impact of a 40% reduction in cell resistance compared to the results of this study in Figure 9 (dark shading; also see Figure 2C). Currently, Ir-PD targets are defined based on catalyst loading relative to power output. However, reducing cell resistance, which is of prime importance to reach high current density, is primarily achieved through improvements in components other than the catalyst. Achieving the DOE target will likely result in Ir-PD values below 0.1 mg_{Ir} W^{-1} as long as iridium loadings remain below 0.52 mg_{Ir} cm^{-2}. An alternative path to meet these Ir-PD values is to sacrifice efficiency in favor of maximizing current density. From this perspective, iridium scarcity appears to be less of a performance-limiting factor. In contrast, durability presents a greater challenge, as it depends not only on stable materials but also on a deep understanding of how operational strategies affect system lifetime. While recent research has heavily focused on catalyst design, catalyst integration and component interactions remain underexplored yet are increasingly critical for industrial-scale deployment.

Focusing solely on iridium performance in terms of Ir-PD also allowed us to estimate the technically feasible market share of PEMWE electrolyzers, based on the experimental data from this study (Figure 9B). Adapting the method proposed by Clapp et al. (supplemental information), the maximum technically feasible PEMWE market share was calculated as a function of the achieved Ir-PD while assuming a global iridium supply of 1.5 t_{Ir} per year allocated to PEMWE. A system energy efficiency of 48 kWh kg_{H2}^{-1} was assumed, though this parameter has only a minor influence on Ir-PD-based market share estimations. We calculated the average and standard deviation of the low-emissions hydrogen balance (in Mt H_2 equivalent) based on the 2022–2024 projections for both the APS and NZE scenarios, for the years 2030 and 2050.[56–58] The lowest Ir-PD values achieved in this study were 0.048 mg_{Ir} W^{-1} at 2 V (0.091 mg_{Ir} W^{-1} at 1.8 V) for 0.4 mg_{Ir} cm^{-2} and 0.015 mg_{Ir} W^{-1} using a loading of 0.1 mg_{Ir} cm^{-2}. Figure 9B shows that, from a performance standpoint, these Ir-PD values support achieving reasonable PEMWE market shares if performance is maintained throughout the stack's lifetime. However, large uncertainties persist, particularly concerning future H_2 demand and the pace of the market ramp-up. These factors significantly influence the required iridium resources and may lead to an overestimation of pressure on global iridium availability.

The predictions presented are just one focal point within a much broader context. Discussing material efficiency is crucial in terms of environmental impact but also with respect to the corresponding costs. The latter is particularly relevant, as iridium remains a major cost driver for stacks.[59] Encouragingly, the current discourse on iridium availability, recyclability, and circularity, occurring prior to full market penetration, may ultimately support the deployment of PEMWE systems. This should be extended to all components and other electrolyzer technologies.

In this study, several commercial catalysts were evaluated for their loading-dependent performance and corresponding durability. The most robust catalyst-specific conclusions rest on three independent lines of evidence largely insensitive to membrane-dominated HFR variability: the continuous evolution of R_{ct} extracted from EIS, which directly reflects kinetic degradation at the catalyst layer. Postmortem XPS analysis independently confirmed progressive crystallization toward a more rutile-like structure in the amorphous catalysts, corroborating the electrochemical trends. The fundamentally different behavior of Elyst Ir75 0480 across both metrics serves as an internal

reference, confirming that the observed trends are catalyst specific rather than artifacts of assembly or test station variability. The convergence of these three independent datasets provides a robust basis for the conclusions drawn despite the inherent variability of device-level testing.

Overall, the results suggest that durability assessment efforts should be strengthened, while catalyst development should focus on stability, integration, and interfacial interactions rather than solely on peak performance. As Ir-PD targets appear attainable using SoA materials, the research bottleneck shifts toward lifetime and operational strategy. The durability testing showed that each catalyst and loading combination exhibited distinct behavior, and degradation rates decreased with extended testing time. This underlines the importance of operational strategy, which may be more impactful than novel catalyst design. Greater attention must be given to catalyst integration within the catalyst layer and to component interactions throughout the cell. The discussion around iridium material efficiency also contributes to sustainability-by-design principles and should be extended to other system components and related technologies.

METHODS

Materials and components

We selected four commercially available iridium-based catalysts from three different suppliers for this study: H2EL-45IrO-S60 and H2EL-IrO (both Heraeus), Elyst Ir75 0480 (Umicore), and Premion (Alfa Aesar). For the anode PTL, a titanium felt was used (2GDL10–0.35, Bekaert), while for the cathode, a carbon PTL (TGP-H-120, Toray) was used. The thickness of both PTL types was determined using a custom-built device that measured each PTL at four points simultaneously. The anode PTL thickness ranged from 355 to 360 μm, while the cathode PTL ranged from 360 to 365 μm. Thickness data for both PTL types are shown in Figure S7, with the selected range indicated by dashed lines.

The thickness of the PTFE gasket was determined using a fixed-position thickness gauge (DM 2010, Wolf Messtechnik GmbH), with measurements taken at three positions per gasket. The anode gasket thickness matched that of the Ti-PTL, consistently ranging from 355 to 360 μm, while the cathode gasket thickness ranged from 250 to 255 μm.

For the performance screening, the anode PTL was reused, while new gaskets and a new carbon PTL were used for each test. In contrast, each durability test was conducted using new anode and cathode PTLs together with corresponding new gaskets. The membrane was an N115 Nafion membrane purchased from Chemours.

CCM fabrication

Ultrasonic spray coating

Catalyst dispersions were prepared by adding the specified catalyst (Premion, H2EL-45IrO-S60, and Elyst Ir75 0480) into a 100 mL laboratory bottle. Deionized water (Milli-Q, Merck Millipore) was added first, followed by n-propanol (Merck), yielding a final catalyst concentration of 3.3 mg mL^{-1}. The dispersion was cooled in an ice bath for 5 min prior to the addition of the water-based Nafion ionomer dispersion (D1021, Ion Power). The mixture was then sonicated using an ultrasonic horn (Bandelin, Sonopuls HD 2200, amplitude 50%, KE76) while placed in an ice bath. A modified recipe was employed for H2EL-IrO. The catalyst was first pre-mixed with the Nafion ionomer dispersion using a rolling bank to ensure uniform distribution. A 1:9 (v/v) water/n-propanol mixture was then added. This dispersion was subsequently subjected to the same ultrasonic treatment as the other formulations. PSDs of the dispersions were characterized using an acoustic spectrometer (DT-1202, 3P Instruments). The catalyst layers were deposited onto a PTFE-coated glass silk fabric substrate using an ultrasonic spray-coating system (ExactaCoat, Sono-Tek) equipped with an integrated AccuMist nozzle operating at 48 kHz. A 25 mL Hamilton precision syringe was used to dispense 0.2 mL min^{-1} via a Sono-Tek syringe pump controlled by the ExactaCoat software. Four catalyst layers were sprayed at once. The substrate was placed on a vacuum plate heated to 90°C during deposition. Iridium loadings were determined gravimetrically using a precision balance (AG204, Mettler Toledo). The final catalyst layers exhibited iridium loadings between 0.1 and 0.9 mg_{Ir} cm^{-2}.

Doctor-blade-coating process

The cathode catalyst dispersion was prepared by first mixing the dry powder with ultrapure water, then adding 2-butanol and further mixing. A 15 wt % isopropanol-based ionomer dispersion (LQ-1115, Ion Power) was then added. The resulting mixture was cooled on ice and homogenized using an ultrasonic horn (Bandelin, Sonopuls HD 3400, amplitude 20%, MS73) for 5 min. The prepared dispersion was applied to the decal substrate using a universal film applicator (ZUA2000, Zehntner) with a wet film thickness of 55 μm to achieve a platinum loading of 0.14 ± 0.03 mg_{Pt} cm^{-2} and a Nafion content of 20 wt %. The samples were air-dried for 30 min, then oven-dried at 60°C for 3 h.

Decal process

The CCMs were fabricated by hot pressing the N115 membrane between the cathode and anode decals at 150°C, using a 13 min pre-heating phase and 3 min of pressure at 1.9 kN cm^{-2}.

Single-cell testing

Testing hardware

An in-house cell was used (17.64 cm^2) for all tests. The performance assessment was conducted on a Greenlight E100 while the durability tests were performed with a custom-built multichannel test station.[60] The cell was assembled by tightening the bolts in two torque steps: first to 4 Nm, then to 8 Nm. Based on the material dimensions described above, the cathode PTL compression was 110 μm, corresponding to approximately 31% of its initial thickness.

Water quality was controlled using an ion exchanger, which typically produced conductivity values below 0.3 μS cm^{-1} at the beginning of operation. Its long-term behavior under comparable operating conditions is well established. Therefore, significant effects from water impurities are considered unlikely.

Performance assessment

Warm-up and cell-conditioning procedures were performed according to previously established protocols.[28] Performance evaluation was conducted using polarization curves with a

hold time of 5 min per point, starting at 1.45 V. In the low-voltage region (1.45–1.55 V), the potential was increased in 0.01 V steps, followed by 0.05 V steps for potentials above 1.55 V. The forward scan was terminated at 2.00 V and immediately followed by a reverse scan using the same stepwise protocol. This measurement cycle was repeated ten times to ensure consistency and reproducibility. A protective voltage of 1.2 V was used in all idle phases. EIS (Biologic HCP-1005 with 100A booster) was performed over the frequency range 10 kHz to 100 mHz at an amplitude of 5 mV.

The 500 h durability assessment initially followed the same procedure as the performance screening. The durability test began with a galvanostatic operation at 2 A cm^{-2} for 100 h, followed by a quite harsh dynamic durability test consisting of a loop of 4,500 triangular cycles between 1.45 and 1.99 V at a scan rate of 30 mV s^{-1}. The loop was repeated seven times. Then, another galvanostatic operation at a constant current density of 2 A cm^{-2} was performed for 100 h. Polarization curves and EIS measurements were recorded between each galvanostatic phase and loop. The dynamic cycling procedure lasted 320 h and included 31,500 total cycles. Together with both galvanostatic phases, the durability test takes 520 h, plus additional time for performance analysis. This methodology, which is intended to be stressful for the catalysts, was adapted from Alia et al.[61] and the EU harmonized stress-testing protocol.[62]

Durability 1,000 h testing

The extended durability test was conducted as the 500 h test but with longer cycling between the two 100 h galvanostatic phases. There were 81,000 total cycles, and the total cycling time was 810 h, resulting in a total stress test period of 1,010 h.

Data treatment

The forward scan of the tenth polarization curve was used as the performance metric. Polarization curve analysis was consistently based on the forward scan, with the last ten data points at each set point averaged to ensure stable evaluation. Comparison of forward and backward scans showed no significant hysteresis and was used as an additional quality control measure. All polarization curve data were corrected for HFR to remove dominant membrane- and assembly-related ohmic contributions, enabling catalyst-layer-specific performance evaluation. The Ir-PD was calculated for all catalysts, loadings, and durability phases following the procedure described in the supplemental information. Degradation rates were extracted by linear regression of the HFR-corrected performance data at a given LHV over three distinct operational intervals: the total test period (BoL to EoL), the dynamic cycling phase, and the galvanostatic phases.

Physicochemical characterization

The PSD was measured with a Malvern Mastersizer 3000 (laser diffraction) with a Hydro SV module (small-volume module). To determine the surface area, N2 physisorption on a Gemini VII from Micromeritics was performed and evaluated using the BET (Brunauer-Emmett-Teller) approach of the related software. The XRD patterns were measured using a D8 DISCOVER (Bruker) with a Cu Kα source and LYNXEYE_XE_T as a detector. TPR measurements of the powders were performed using a Micromeritics AutoChem III with 100 mg of catalyst in 5 vol % H_2 in Ar (50 sccm, 2.2 mmol min^{-1}). The sample was loaded into a U-shaped quartz reactor and flushed with argon before being heated. The temperature increased at a rate of 10°C min^{-1} up to 700°C, and H2 consumption was monitored via a thermal conductivity detector. XPS measurements were performed using a PHI 5000 VersaProbe II system (ULVAC-PHI, USA) equipped with a monochromatic Al Kα X-ray source ($h\nu$ = 1.486 keV). The X-ray settings were 50 W and 15 kV, with a spot size of 200 μm. For both powder samples and CCMs, survey spectra were acquired at a pass energy of 187.5 eV with a step size of 0.8 eV and a dwell time of 100 ms per step. High-resolution spectra were recorded at a pass energy of 23.5 eV, with a step size of 0.1 eV and the same dwell time. Quantification was performed in atom percent (atom %) with an estimated error of ≥10% and normalized to a total of 100 atom %. Background subtraction was conducted using the Shirley method, and empirical relative sensitivity factors were applied. For powder samples, charge correction was applied by referencing the main C 1s component to 285.0 eV. For CCM samples, the correction was performed by setting the CF_2 component of the C 1s signal to 292.2 eV. Following the procedure outlined by Roiron et al., the XPS data were integrated, and the resulting iridium oxidation state and oxygen species ratios ($Ir^{3+}/Ir^{4+}$and μ_1-O/μ_2-O) were used to distinguish between more crystalline and more amorphous catalysts.[49]

Cross-sectional analyses of the CCMs were performed with the specified SEM. Ten cross-sectional images were used to determine the thickness distribution of the pristine catalyst layers and after the durability test. The thickness distribution was determined using a previously published method that was adapted to the specific needs arising from the deformed CCM surface. This modified method is described in the supplemental information. Outliers in the analysis of catalyst layer thickness were identified and excluded using standard interquartile range criteria (Q1 − 1.5 IQR and Q3 + 1.5 IQR). No outlier removal was applied to the electrochemical datasets. The elemental composition of the powders and CCMs was analyzed via EDX using a Zeiss Gemini Ultra Plus system. The system operated at an accelerating voltage of 20 kV to ensure sufficient excitation of characteristic X-ray emissions.

The sheet resistance and the thickness distribution of the catalyst layers were determined using a previously published method.[63] The catalyst-layer sheet resistances were measured exclusively for the pristine catalyst layers deposited on the N115 membrane. Four-point probe analysis was conducted at an optimized compression force of approximately 1,700 N, which was determined through repeated measurements and statistical analysis. The measurements were taken in a controlled climate chamber at 25°C and 25% relative humidity (RH) using a potentiostat (SP-50, Biologic) combined with a custom-built relay switching device. The device was validated using commercial reference measurements. Linear potential scans were applied from 0 to 5 mV at a rate of 0.5 mV s^{-1}. Sheet resistance was determined by linear fitting of the resulting current-voltage response. The results were averaged over multiple probe positions to account for local variability. Thickness-normalized resistance values were determined using the mean catalyst-layer thickness from the thickness analysis.

Statistical analysis

Data evaluation was conducted using Python-based analytical tools, including SciPy, NumPy, Pandas, and Matplotlib for plotting. Results presented with error margins or visualized with error bars reflect the arithmetic mean accompanied by the standard deviation (mean ± SD).

RESOURCE AVAILABILITY

Lead contact

Requests for further information and resources should be directed to the lead contact, Nikolai Utsch (n.utsch@fz-juelich.de).

Materials availability

All catalysts and cell components used are commercially available, and no new materials were generated within this study.

Data and code availability

- All data underlying the figures reported in this paper are publicly available on Jülich DATA (https://data.fz-juelich.de). Further raw data supporting the findings of this study are available from the lead contact upon reasonable request.
- The image analysis code for catalyst-layer thickness determination will be made publicly available on Zenodo (https://doi.org/10.5281/zenodo.20706574) upon publication of this work.

ACKNOWLEDGMENTS

We are grateful to Dr. Quoc Khanh Tran for performing the TPR measurements. The authors gratefully acknowledge that open access publication of this work was funded through the German Project DEAL agreement.

AUTHOR CONTRIBUTIONS

Conceptualization, N.U., F.S., and D.A.-P.; methodology, N.U., F.S., and D.A.-P.; investigation, N.U. and H.H.; formal analysis, N.U., F.S., D.A.-P., and H.H.; data curation, N.U.; visualization, N.U.; project administration, N.U., D.A.-P., and M.M.; writing – original draft, N.U.; writing – review & editing, N.U., F.S., D.A.-P., H.H., M.M., and R.P.; funding acquisition, D.A.-P. and R.P.; resources, M.M. and R.P.; and supervision, N.U., F.S., D.A.-P., M.M., and R.P.

DECLARATION OF INTERESTS

The authors declare that they have no competing interests. They also declare that they have no personal relationships that could have appeared to influence the work reported in this paper.

SUPPLEMENTAL INFORMATION

Supplemental information can be found online at https://doi.org/10.1016/j.xcrp.2026.103441.

Received: January 23, 2026
Revised: May 17, 2026
Accepted: June 26, 2026

REFERENCES

1. Hertwich, E., Lifset, R., Pauliuk, S., Heeren, N., Ali, S., Tu, Q., Ardente, F., Berrill, P., Fishman, T., Kanaoka, K., et al. (2020). Resource Efficiency and Climate Change: Material Efficiency Strategies for a Low-Carbon Future (IRP). https://doi.org/10.5281/ZENODO.3542680.
2. Hertwich, E.G. (2021). Increased Carbon Footprint of Materials Production Driven by Rise in Investments. Nat. Geosci. *14*, 151–155. https://doi.org/10.1038/s41561-021-00690-8.
3. Intergovernmental Panel On Climate Change (2019). Climate Change and Land: IPCC Special Report on Climate Change, Desertification, Land Degradation, Sustainable Land Management, Food Security, and Greenhouse Gas Fluxes in Terrestrial Ecosystems, 1st ed. (Cambridge University Press). https://doi.org/10.1017/9781009157988.
4. Giljum, S., Maus, V., Sonter, L., Luckeneder, S., Werner, T., Lutter, S., Gershenzon, J., Cole, M.J., Siqueira-Gay, J., and Bebbington, A. (2025). Metal Mining Is a Global Driver of Environmental Change. Nat. Rev. Earth Environ. *6*, 441–455. https://doi.org/10.1038/s43017-025-00683-w.
5. Schlichenmaier, S., and Naegler, T. (2022). May Material Bottlenecks Hamper the Global Energy Transition towards the 1.5 °C Target? Energy Rep. *8*, 14875–14887. https://doi.org/10.1016/j.egyr.2022.11.025.
6. Naegler, T., Rauner, S., Dirnaichner, A., Jochem, P., Schlosser, S., and Luderer, G. (2025). Raw Material Demand and Geopolitical Risk in Carbon-Neutral Futures. Energy Policy *204*, 114622. https://doi.org/10.1016/j.enpol.2025.114622.
7. Factsheet Platinum Group Metals (2023). SCRREEN - Solutions for CRitical Raw materials - a European Expert Network. PLATINUM GROUP METALS. https://scrreen.eu/wp-content/uploads/2023/08/SCRREEN2_factsheets_PGM.pdf.
8. Manfredi, S. Raw Materials Information System (RMIS). JRC Publications Repository. https://publications.jrc.ec.europa.eu/repository/handle/JRC118579 (accessed 2025-07-23).
9. Wang, C., Lee, K., Liu, C.P., Kulkarni, D., Atanassov, P., Peng, X., and Zenyuk, I.V. (2024). Design of PEM Water Electrolysers with Low Iridium Loading. Int. Mater. Rev. *69*, 3–18. https://doi.org/10.1177/09506608231216665.
10. European Commission. Joint Research Centre (2023). Supply Chain Analysis and Material Demand Forecast in Strategic Technologies and Sectors in the EU: A Foresight Study (Publications Office: LU).
11. Clapp, M., Zalitis, C.M., and Ryan, M. (2023). Perspectives on Current and Future Iridium Demand and Iridium Oxide Catalysts for PEM Water Electrolysis. Catal. Today *420*, 114140. https://doi.org/10.1016/j.cattod.2023.114140.
12. Graedel, T.E., Allwood, J., Birat, J.-P., Reck, B.K., Sibley, S.F., Sonnemann, G., Buchert, M., and Hagelüken, C. (2011). Recycling Rates of Metals – A Status Report. A Report of the Working Group on Global Metal Flows to the International Resource Panel (UNEP).
13. Carmo, M., Keeley, G.P., Holtz, D., Grube, T., Robinius, M., Müller, M., and Stolten, D. (2019). PEM Water Electrolysis: Innovative Approaches towards Catalyst Separation, Recovery and Recycling. Int. J. Hydrogen Energy *44*, 3450–3455. https://doi.org/10.1016/j.ijhydene.2018.12.030.
14. Kim, TY, Gould, T, Bennet, S, Briens, F, Dasgupta, A, Gonzales, P, Gouy, A, Kamiya, G, Karpiniski, M, Lagelee, J. The Role of Critical Minerals in Clean Energy Transitions. International Energy Agency.
15. Glaister, B.J., and Mudd, G.M. (2010). The Environmental Costs of Platinum–PGM Mining and Sustainability: Is the Glass Half-Full or Half-Empty? Miner. Eng. *23*, 438–450. https://doi.org/10.1016/j.mineng.2009.12.007.
16. Johnson, E.L., Ericsson, M., and Löf, A. (2023). The Mining Permitting Process in Selected Developed Economies. Land Use Policy *131*, 106762. https://doi.org/10.1016/j.landusepol.2023.106762.
17. Söderholm, P. (2023). How Environmental Permitting Uncertainty in Large-Scale Mining Could Influence Subcontractors: The Underlying Chicken-and-Egg Problem. Resour. Policy *82*, 103585. https://doi.org/10.1016/j.resourpol.2023.103585.
18. Igogo, T., Awuah-Offei, K., Newman, A., Lowder, T., and Engel-Cox, J. (2021). Integrating Renewable Energy into Mining Operations: Opportunities, Challenges, and Enabling Approaches. Appl. Energy *300*, 117375. https://doi.org/10.1016/j.apenergy.2021.117375.

19. Georgitzikis, G., Eynard, S., Bobba, S., Perpetuo Coelho, F., Ingoglia, D., and Garbossa, E. (2023). *Platinum: Impact Assessment for Supply Security*; Scientific Analysis or Review, Anticipation and Foresight (European Commission).

20. Odenweller, A., and Ueckerdt, F. (2025). The Green Hydrogen Ambition and Implementation Gap. Nat. Energy *10*, 110–123. https://doi.org/10.1038/s41560-024-01684-7.

21. Terlouw, T., Rosa, L., Bauer, C., and McKenna, R. (2024). Future Hydrogen Economies Imply Environmental Trade-Offs and a Supply-Demand Mismatch. Nat. Commun. *15*, 7043. https://doi.org/10.1038/s41467-024-51251-7.

22. C. Gollier and D. Rohner, eds. (2023). Peace Not Pollution: How Going Green Can Tackle Both Climate Change and Toxic Politics (CEPR Press).

23. Mertens, J., Dewulf, J., Breyer, C., Belmans, R., Gendron, C., Geoffron, P., Goossens, L., Fischer, C., Du Fornel, E., Hayhoe, K., et al. (2024). From Emissions to Resources: Mitigating the Critical Raw Material Supply Chain Vulnerability of Renewable Energy Technologies. Miner. Econ. *37*, 669–676. https://doi.org/10.1007/s13563-024-00425-2.

24. Minke, C., Suermann, M., Bensmann, B., and Hanke-Rauschenbach, R. (2021). Is Iridium Demand a Potential Bottleneck in the Realization of Large-Scale PEM Water Electrolysis? Int. J. Hydrogen Energy *46*, 23581–23590. https://doi.org/10.1016/j.ijhydene.2021.04.174.

25. Bernt, M., Siebel, A., and Gasteiger, H.A. (2018). Analysis of Voltage Losses in PEM Water Electrolyzers with Low Platinum Group Metal Loadings. J. Electrochem. Soc. *165*, F305–F314. https://doi.org/10.1149/2.0641805jes.

26. Taie, Z., Peng, X., Kulkarni, D., Zenyuk, I.V., Weber, A.Z., Hagen, C., and Danilovic, N. (2020). Pathway to Complete Energy Sector Decarbonization with Available Iridium Resources Using Ultralow Loaded Water Electrolyzers. ACS Appl. Mater. Interfaces *12*, 52701–52712. https://doi.org/10.1021/acsami.0c15687.

27. Bernt, M., Hartig-Weiß, A., Tovini, M.F., El-Sayed, H.A., Schramm, C., Schröter, J., Gebauer, C., and Gasteiger, H.A. (2020). Current Challenges in Catalyst Development for PEM Water Electrolyzers. Chem. Ing. Tech. *92*, 31–39. https://doi.org/10.1002/cite.201900101.

28. Bender, G., Carmo, M., Smolinka, T., Gago, A., Danilovic, N., Mueller, M., Ganci, F., Fallisch, A., Lettenmeier, P., Friedrich, K.A., et al. (2019). Initial Approaches in Benchmarking and Round Robin Testing for Proton Exchange Membrane Water Electrolyzers. Int J Hydrogen Energ *44*, 9174–9187. https://doi.org/10.1016/j.ijhydene.2019.02.074.

29. Lickert, T., Fischer, S., Young, J.L., Klose, S., Franzetti, I., Hahn, D., Kang, Z., Shviro, M., Scheepers, F., Carmo, M., et al. (2023). Advances in Benchmarking and Round Robin Testing for PEM Water Electrolysis: Reference Protocol and Hardware. Appl. Energy *352*, 121898. https://doi.org/10.1016/j.apenergy.2023.121898.

30. Fortiner, S., Ouimet, R., Young, J.L., Bender, G., Carmo, M., and Ayers, K. (2025). A Harmonized Protocol to Assess the Single-Cell Performance of Proton Exchange Membrane Water Electrolyzers. Front. Energy Res. *13*, 1549219. https://doi.org/10.3389/fenrg.2025.1549219.

31. Parimuha, M.R., Young, J.L., Lee, J.K., Yilmaz, A., Diaz-Abad, S., Gawas, R., Schuler, T., Komini Babu, S., and Bender, G. (2025). Proton Exchange Membrane Electrolysis Benchmarking: Identifying and Removing Sources of Variation in Test Stations, Hardware, and Membrane Electrode Assembly Fabrication. Int. J. Hydrogen Energy *114*, 486–496. https://doi.org/10.1016/j.ijhydene.2025.02.443.

32. Bautkinova, T., Utsch, N., Bystron, T., Lhotka, M., Kohoutkova, M., Shviro, M., and Bouzek, K. (2023). Introducing Titanium Hydride on Porous Transport Layer for More Energy Efficient Water Electrolysis with Proton Exchange Membrane. J. Power Sources *565*, 232913. https://doi.org/10.1016/j.jpowsour.2023.232913.

33. Alia, S.M., Reeves, K.S., Yu, H., Park, J.H., Kariuki, N.N., Kropf, A.J., Myers, D.J., and Cullen, D.A. (2024). Catalyst-Specific Accelerated Stress Tests in Proton Exchange Membrane Low-Temperature Electrolysis for Intermittent Operation. J. Electrochem. Soc. *171*, 024505. https://doi.org/10.1149/1945-7111/ad2735.

34. Bernt, M., and Gasteiger, H.A. (2016). Influence of Ionomer Content in IrO2/TiO2Electrodes on PEM Water Electrolyzer Performance. J. Electrochem. Soc. *163*, F3179–F3189. https://doi.org/10.1149/2.0231611jes.

35. Strategic Research and Innovation Agenda - Clean Hydrogen Partnership. https://www.clean-hydrogen.europa.eu/about-us/key-documents/strategic-research-and-innovation-agenda_en (accessed 2025-07-25).

36. Pivovar, B.; Ruth, M.; Ahluwalia, R. H2NEW: Hydrogen (H2) from Next-Generation Electrolyzers of Water LTE Task 3c: System and Techno-Economic Analysis. National Renewable Energy Laboratory.

37. Darge, P.L., Röttcher, N.C., Zlatar, M., Mayrhofer, K.J.J., Cherevko, S., and Dworschak, D. (2025). Shortening Accelerated Stress Tests: An Identical Charge Approach for Oxygen Evolution Reaction Electrocatalysts. ACS Catal. *15*, 10336–10346. https://doi.org/10.1021/acscatal.5c01464.

38. Zlatar, M., Escalera-López, D., Simon, C., Briega-Martos, V., Stojanovski, K., and Cherevko, S. (2025). Dependence of Noble Metals Dissolution: Iridium. Electrochim. Acta *513*, 145450. https://doi.org/10.1016/j.electacta.2024.145450.

39. Weiß, A., Siebel, A., Bernt, M., Shen, T.H., Tileli, V., and Gasteiger, H.A. (2019). Impact of Intermittent Operation on Lifetime and Performance of a PEM Water Electrolyzer. J. Electrochem. Soc. *166*, F487–F497. https://doi.org/10.1149/2.0421908jes.

40. Geuß, M., Löttert, L., Böhm, T., Hutzler, A., Mayrhofer, K.J.J., Thiele, S., and Cherevko, S. (2024). Quantification of Iridium Dissolution at Water Electrolysis Relevant Conditions Using a Gas Diffusion Electrode Half-Cell Setup. ACS Catal. *14*, 11819–11831. https://doi.org/10.1021/acscatal.4c02159.

41. Röttcher, N.C., Zhou, J., Löttert, L., Mayrhofer, K.J.J., and Dworschak, D. (2025). Tracing Iridium Dissolution Pathways in Proton Exchange Membrane Water Electrolyzers at Relevant Current Densities in Real Time. Chemelectrochem *12*, e202500098. https://doi.org/10.1002/celc.202500098.

42. Schalenbach, M., Wolf, N., Poc, J.-P., Heume, C., Basak, S., Schierholz, R., Karl, A., Jodat, E., and Eichel, R.-A. (2025). Accelerated Iridium Dissolution in Proton Exchange Membrane (PEM) Water Electrolyzers by Inert Mobile Anions Adsorbed in the Double Layer. J. Electrochem. Soc. *172*, 064509. https://doi.org/10.1149/1945-7111/ade0ef.

43. Milosevic, M., Böhm, T., Körner, A., Bierling, M., Winkelmann, L., Ehelebe, K., Hutzler, A., Suermann, M., Thiele, S., and Cherevko, S. (2023). Search of Lost Iridium: Quantification of Anode Catalyst Layer Dissolution in Proton Exchange Membrane Water Electrolyzers. ACS Energy Lett. *8*, 2682–2688. https://doi.org/10.1021/acsenergylett.3c00193.

44. Alia, S.M., Reeves, K.S., Cullen, D.A., Yu, H., Kropf, A.J., Kariuki, N., Park, J.H., and Myers, D.J. (2024). Simulated Start-Stop and the Impact of Catalyst Layer Redox on Degradation and Performance Loss in Low-Temperature Electrolysis. J. Electrochem. Soc. *171*, 044503. https://doi.org/10.1149/1945-7111/ad2bea.

45. Zeng, Z., Ouimet, R., Bonville, L., Niedzwiecki, A., Capuano, C., Ayers, K., Soleymani, A.P., Jankovic, J., Yu, H., Mirshekari, G., et al. (2022). Degradation Mechanisms in Advanced MEAs for PEM Water Electrolyzers Fabricated by Reactive Spray Deposition Technology. J. Electrochem. Soc. *169*, 054536. https://doi.org/10.1149/1945-7111/ac7170.

46. Stähler, M., Burdzik, A., Friedrich, I., Everwand, A., and Scheepers, F. (2024). Oxygen Flow Rate Measurement as a Whistleblower for Degradation Effects in PEM Water Electrolysis. Int. J. Hydrogen Energy *78*, 682–687. https://doi.org/10.1016/j.ijhydene.2024.06.334.

47. Mom, R.V., Falling, L.J., Kasian, O., Algara-Siller, G., Teschner, D., Crabtree, R.H., Knop-Gericke, A., Mayrhofer, K.J.J., Velasco-Vélez, J.-J., and Jones, T.E. (2022). Operando Structure–Activity–Stability Relationship of Iridium Oxides during the Oxygen Evolution Reaction. ACS Catal. *12*, 5174–5184. https://doi.org/10.1021/acscatal.1c05951.

48. Geiger, S., Kasian, O., Ledendecker, M., Pizzutilo, E., Mingers, A.M., Fu, W.T., Diaz-Morales, O., Li, Z., Oellers, T., Fruchter, L., et al. (2018). The Stability Number as a Metric for Electrocatalyst Stability Benchmarking. Nat. Catal. *1*, 508–515. https://doi.org/10.1038/s41929-018-0085-6.

49. Roiron, C., Wang, C., Zenyuk, I.V., and Atanassov, P. (2024). Oxygen 1s X-Ray Photoelectron Spectra of Iridium Oxides as a Descriptor of the Amorphous–Rutile Character of the Surface. J. Phys. Chem. Lett. *15*, 11217–11223. https://doi.org/10.1021/acs.jpclett.4c02616.

50. Zlatar, M., Xie, X., Franke, C., Hrbek, T., Krtouš, Z., Li, T., Khalakhan, I., and Cherevko, S. (2025). On the Growth and Water Oxidation Stability of Hydrous Iridium Oxide. EES Catal. *3*, 521–534, D4EY00268G. https://doi.org/10.1039/D4EY00268G.

51. Nong, H.N., Falling, L.J., Bergmann, A., Klingenhof, M., Tran, H.P., Spöri, C., Mom, R., Timoshenko, J., Zichittella, G., Knop-Gericke, A., et al. (2020). Key Role of Chemistry versus Bias in Electrocatalytic Oxygen Evolution. Nature *587*, 408–413. https://doi.org/10.1038/s41586-020-2908-2.

52. Pfeifer, V., Jones, T.E., Velasco Vélez, J.J., Massué, C., Greiner, M.T., Arrigo, R., Teschner, D., Girgsdies, F., Scherzer, M., Allan, J., et al. (2016). The Electronic Structure of Iridium Oxide Electrodes Active in Water Splitting. Phys. Chem. Chem. Phys. *18*, 2292–2296. https://doi.org/10.1039/C5CP06997A.

53. Yonkova, V., Utsch, N., Borowec, J., Eichel, R.-A., Hausen, F., Scheepers, F., Brinckmann, S., and Schwaiger, R. (2024). Comparative Analysis and Error Assessment of Nanoindentation Evaluation Techniques for NafionTM117. JOM *76*, 2315–2325. https://doi.org/10.1007/s11837-024-06485-7.

54. Hintzen, A., Stähler, M., and Friedrich, I. (2025). Membrane Creep Caused by Porous Transport Layer Compression in PEM Water Electrolysis and the Impact on Hydrogen Permeation. J. Electrochem. Soc. *172*, 044512. https://doi.org/10.1149/1945-7111/adcd00.

55. Dzara, M.J., Artyushkova, K., Foster, J., Eskandari, H., Chen, Y., Mauger, S.A., Atanassov, P., Karan, K., and Pylypenko, S. (2024). X-Ray Photoelectron Spectroscopy Analysis of Nafion-Containing Samples: Pitfalls, Protocols, and Perceptions of Physicochemical Properties. J. Phys. Chem. C *128*, 8467–8482. https://doi.org/10.1021/acs.jpcc.4c00872.

56. World Energy Outlook 2022 – Analysis. IEA. https://www.iea.org/reports/world-energy-outlook-2022 (accessed 2025-07-23).

57. World Energy Outlook 2023 – Analysis. IEA. https://www.iea.org/reports/world-energy-outlook-2023 (accessed 2025-07-23).

58. World Energy Outlook 2024 – Analysis. IEA. https://www.iea.org/reports/world-energy-outlook-2024 (accessed 2025-07-23).

59. Badgett, A., Brauch, J., Thatte, A., Rubin, R., Skangos, C., Wang, X., Ahluwalia, R., Pivovar, B., and Ruth, M. (2024). Updated Manufactured Cost Analysis for Proton Exchange Membrane Water Electrolyzers (National Renewable Energy Laboratory). https://doi.org/10.2172/2311140.

60. Liu, C., Shviro, M., Gago, A.S., Zaccarine, S.F., Bender, G., Gazdzicki, P., Morawietz, T., Biswas, I., Rasinski, M., Everwand, A., et al. (2021). Exploring the Interface of Skin-Layered Titanium Fibers for Electrochemical Water Splitting. Adv. Energy Mater. *11*, 2002926. https://doi.org/10.1002/aenm.202002926.

61. Alia, S.M., Stariha, S., and Borup, R.L. (2019). Electrolyzer Durability at Low Catalyst Loading and with Dynamic Operation. J. Electrochem. Soc. *166*, F1164–F1172. https://doi.org/10.1149/2.0231915jes.

62. European Commission. Joint Research Centre (2024). EU Harmonised Accelerated Stress Testing Protocols for Low-Temperature Water Electrolyser: A Proposal with Testing Guidance for Assessing Performance Degradation in Water Electrolyser Stacks (Publications Office: LU).

63. Utsch, N., Berg, F., Scheepers, F., Holtwerth, S., Shviro, M., Lehnert, W., and Mechler, A.K. (2025). Innovative Method for Reliable Measurement of PEM Water Electrolyzer Component Resistances. Small Methods *9*, 2401842. https://doi.org/10.1002/smtd.202401842.